

THE LUMINOSITY FUNCTION OF EARLY-TYPE FIELD GALAXIES AT  $Z \approx 0.75$ 

N.J.G. CROSS<sup>1</sup>, R.J. BOUWENS<sup>2</sup>, N. BENÍTEZ<sup>1</sup>, J.P. BLAKESLEE<sup>1</sup>, F. MENANTEAU<sup>1</sup>, H.C. FORD<sup>1</sup>,  
 T. GOTO<sup>1</sup>, B. HOLDEN<sup>2</sup>, A.R. MARTEL<sup>1</sup>, A. ZIRM<sup>3</sup>, R. OVERZIER<sup>3</sup>, C. GRONWALL<sup>4</sup>, N.  
 HOMEIER<sup>1</sup>, D.R. ARDILA<sup>1</sup>, F. BARTKO<sup>5</sup>, T.J. BROADHURST<sup>6</sup>, R.A. BROWN<sup>7</sup>, C.J. BURROWS<sup>7</sup>,  
 E.S. CHENG<sup>8</sup>, M. CLAMPIN<sup>8</sup>, P.D. FELDMAN<sup>1</sup>, M. FRANX<sup>3</sup>, D.A. GOLIMOWSKI<sup>1</sup>, G.F. HARTIG<sup>7</sup>,  
 G.D. ILLINGWORTH<sup>2</sup>, L. INFANTE<sup>9</sup>, R.A. KIMBLE<sup>8</sup>, J.E. KRIST<sup>7</sup>, M.P. LESSER<sup>10</sup>, G.R. MEURER<sup>1</sup>,  
 G.K. MILEY<sup>3</sup>, M. POSTMAN<sup>1,7</sup>, P. ROSATI<sup>11</sup>, M. SIRIANNI<sup>7</sup>, W.B. SPARKS<sup>7</sup>, H.D. TRAN<sup>12</sup>, Z.I.  
 TSVETANOV<sup>13</sup>, R.L. WHITE<sup>1,7</sup> & W. ZHENG<sup>1</sup>

## ABSTRACT

We measure the luminosity function of morphologically selected E/S0 galaxies from  $z = 0.5$  to  $z = 1.0$  using deep high resolution Advanced Camera for Surveys imaging data. Our analysis covers an area of  $48\text{ arcmin}^2$  ( $8\times$  the area of the HDF-N) and extends 2 magnitudes deeper ( $I \sim 24$  mag) than was possible in the Deep Groth Strip Survey (DGSS). Our fields were observed as part of the ACS Guaranteed Time Observations. At  $0.5 < z < 0.75$ , we find  $M_B^* - 5 \log h_{0.7} = -21.1 \pm 0.3$  and  $\alpha = -0.53 \pm 0.2$ , and at  $0.75 < z < 1.0$ , we find  $M_B^* - 5 \log h_{0.7} = -21.4 \pm 0.2$ , consistent with 0.3 magnitudes of luminosity evolution (from  $0.5 < z < 0.75$ ). These luminosity functions are similar in both shape and number density to the luminosity function using morphological selection (e.g., DGSS), but are much steeper than the luminosity functions of samples selected using morphological proxies like the color or spectral energy distribution (e.g., CFRS, CADIS, or COMBO-17). The difference is due to the ‘blue’,  $(U - V)_0 < 1.7$ , E/S0 galaxies, which make up to  $\sim 30\%$  of the sample at all magnitudes and an increasing proportion of faint galaxies. We thereby demonstrate the need for *both morphological and structural information* to constrain the evolution of galaxies.

We find that the ‘blue’ E/S0 galaxies have the same average sizes and Sersic parameters as the ‘red’,  $(U - V)_0 > 1.7$ , E/S0 galaxies at brighter luminosities ( $M_B < -20.1$ ), but are increasingly different at fainter magnitudes where ‘blue’ galaxies are both smaller and have lower Sersic parameters. We find differences in both the size-magnitude relation and the photometric plane offset for ‘red’ and ‘blue’ E/S0s, although neither ‘red’ nor ‘blue’ galaxies give a good fit to the size magnitude relation. Fits of the colors to stellar population models suggest that most E/S0 galaxies have short star-formation time scales ( $\tau < 1$  Gyr), and that galaxies have formed at an increasing rate from  $z \sim 8$  until  $z \sim 2$  after which there has been a gradual decline.

*Subject headings:* galaxies: elliptical and lenticular, evolution, fundamental parameters, luminosity function

## 1. INTRODUCTION

The luminosity function of galaxies is the number density of galaxies as a function of absolute magnitude. The shape of the luminosity function can be used to constrain galaxy formation models. The luminosity function is often described by three numbers:  $M^*$ , the magnitude at which the number of bright galaxies rapidly decreases;  $\phi^*$ , the space density at  $M^*$ , and the faint end slope  $\alpha$  which characterizes the ratio of dwarf galaxies to giant galaxies. Models of galaxy formation and evolution must be able to account for these parameters, which vary with galaxy type.

Over the past few years, the luminosity function of high redshift ( $z > 0.5$ ) galaxies have been studied extensively through the use of deep, wide-area surveys. Some of the more notable efforts include the Canada-France Redshift Survey (CFRS, Lilly et al. 1995), the Canadian Network for Observational Cosmology Field Galaxy Redshift Survey (CNOC2, Lin et al 1999), the Calar Alto Deep Imaging Survey (CADIS, Fried et al. 2001), the Deep Groth Strip Survey (DGSS, Im et al. 2002), the Subaru Deep Survey (Kashikawa et al. 2003), the Classifying Objects by Medium Band Observations (COMBO-17, Wolf et al.

<sup>1</sup> Department of Physics and Astronomy, Johns Hopkins University, 3400 North Charles Street, Baltimore, MD 21218.

<sup>2</sup> UCO/Lick Observatory, University of California, Santa Cruz, CA 95064.

<sup>3</sup> Leiden Observatory, Postbus 9513, 2300 RA Leiden, Netherlands.

<sup>4</sup> Department of Astronomy and Astrophysics, The Pennsylvania State University, 525 Davey Lab, University Park, PA 16802.

<sup>5</sup> Bartko Science & Technology, P.O. Box 670, Mead, CO 80542-0670.

<sup>6</sup> Racah Institute of Physics, The Hebrew University, Jerusalem, Israel 91904.

<sup>7</sup> STScI, 3700 San Martin Drive, Baltimore, MD 21218.

<sup>8</sup> NASA Goddard Space Flight Center, Laboratory for Astronomy and Solar Physics, Greenbelt, MD 20771.

<sup>9</sup> Departamento de Astronomía y Astrofísica, Pontificia Universidad Católica de Chile, Casilla 306, Santiago 22, Chile.

<sup>10</sup> Steward Observatory, University of Arizona, Tucson, AZ 85721.

<sup>11</sup> European Southern Observatory, Karl-Schwarzschild-Strasse 2, D-85748 Garching, Germany.

<sup>12</sup> W. M. Keck Observatory, 65-1120 Mamalahoa Highway, Kamuela, Hawaii 96743.

<sup>13</sup> NASA Headquarters, Washington, DC 20546-0001.

2003) and from a combination of Hubble Space Telescope (HST) and Very Large Telescope (VLT) images, Poli et al. (2003). Most of these use deep, ground-based images with spectroscopic or photometric redshifts to construct the luminosity function, but do not have the spatial resolution to measure the structural properties of galaxies at higher redshifts.

Without information on the structural properties, ground-based surveys have resorted to using color information as a proxy for morphologies, whether this information comes in the form of a best-fit spectral energy distribution (e.g. Wolf et al. 2003), or a rest-frame color cut (e.g. Lilly et al. 1995). This can result in apparent discrepant results. For example, Wolf et al. (2003) found that the elliptical/S0 (E/S0) galaxies that produce  $\sim 50\%$  cent of the current B-band luminosity density only contributed  $\sim 5\%$  at  $z = 1$ . By contrast, using morphological classification, van den Bergh (2001) found that the fraction of elliptical galaxies has remained constant at  $\sim 17\%$ ,  $0.25 < z < 1.2$ , implying that either the luminosity of ellipticals has increased over time relative to other types of galaxies or that the differences in color-selection and morphological-selection have produced apparently inconsistent results between these surveys.

Surveys using the Hubble Space Telescope (HST) such as the DGSS (Im et al. 2002; Simard et al. 2002) and the Medium Deep Survey (Griffiths et al. 1994) have been able to reliably morphologically classify and measure structural parameters for galaxies with  $I_{AB} < 22$  mag, but over much smaller areas of sky than the deep ground based surveys. These HST surveys have discovered a population of  $0.3 < z < 1$  blue E/S0 galaxies (e.g. Menanteau et al. 1999, Im et al. 2001, Gebhardt et al. 2003) that have similar luminosities to standard red E/S0 galaxies. Im et al. (2001) find these make up  $\sim 15\%$  of the E/S0 sample whereas Menanteau et al. (1999) find a much higher fraction:  $30 - 50\%$  of the sample. Objects such as these demonstrate the inherent weakness of using color as a proxy for morphology. At low redshifts, almost all of the bright E/S0 galaxies are red, with blue ellipticals (dwarf ellipticals) many magnitudes fainter. From the work of Menanteau et al. (2004) and Im et al. (2001) it appears that most of these blue E/S0 galaxies have blue cores and red exteriors, with the exteriors having the same colors as red E/S0 galaxies, which have constant colors at all radii. Im et al. (2001) concluded that these blue E/S0 galaxies were less massive than the red E/S0 galaxies based on the dynamical masses calculated from the velocity dispersions. However, because the velocity dispersions were measured much closer to the core of the galaxy for the low redshift red ellipticals, the high redshift blue ellipticals may be more massive than the measurements suggest. Even if the measurements give accurate dynamical masses, the blue E/S0 galaxies have masses equivalent to the lower mass red E/S0s, so they may still yet evolve into high mass red E/S0s through a combination of luminosity evolution that reddens the stellar population over time and mergers that increase the mass.

Luminosity evolution occurs when there is new star-formation, or when the stellar population ages, and does not necessarily imply any change in the mass or number of stars in a galaxy. Structural parameters such as the size

and shape are better indicators of the morphological evolution, since they are only weakly dependent on the age of the stellar population and are mainly determined by dynamical characteristics such as total mass and angular momentum. Within the half-light radius of a giant elliptical galaxy the dynamical time-scale is very short, less than  $10^8$  years, so dynamical equilibrium is reached very quickly. The size and shape of the galaxy will not change significantly unless mass is added via mergers or accretion; a close encounter changes the angular momentum; tidal forces disrupt the outer layers. Small changes in the apparent shape and size do occur when star-formation is localized in the center, in bars, rings or spiral arms, but these are much weaker changes than the variation in SED or color. Therefore morphology is a more robust indicator of the nature of a galaxy, but it requires good resolution to use.

Previous studies have differed in the way they have utilized size information to make inferences about evolution. Several surveys have assumed that galaxy size and shape are constant with redshift. Schade, Barrientos & Lopez-Cruz (1997) showed that cluster ellipticals evolve as  $\Delta M = -2.85 \log_{10}(1+z)$ , assuming they maintain a constant size, and Schade et al. (1999) demonstrated that field ellipticals show a similar evolution. Using a sample of 44 galaxies with  $z < 2$  Roche et al. (1998) discovered that ellipticals show significant luminosity evolution but little size evolution from  $z = 1.0$  to  $z = 0.2$ . They found that most size evolution appears to happen at  $z > 1.5$ . Graham (2002) compared the scatter in the ‘photometric plane’ which only requires parameters measured from galaxy images, to the scatter in the ‘fundamental plane’ which requires dispersion velocities measured from high resolution spectra. Graham showed that the photometric plane could be used to constrain distances to elliptical galaxies.

In Cross et al. (2001) and Cross & Driver (2002), the effects of surface brightness selection on the  $z = 0$  galaxy luminosity function were discussed. In this paper we look at the LF of morphological early types at  $0.5 < z \leq 1$ . We then examine the effect that color selection has on this luminosity function. Finally, we use structural parameters to test whether blue E/S0 galaxies are progenitors of red E/S0 galaxies and what evolution has taken place from  $z = 1$  to  $z = 0.5$ .

The Advanced Camera for Surveys (ACS, Ford et al. 2002) significantly improves on WFPC2 in terms of sensitivity (a factor of 5), field of view (a factor of 2) and resolution (a factor of 2), giving well sampled PSFs in the  $i$  and  $z$  bands. This leads to significant improvements in both the accuracy of the size measurements and the overall sample size.

In this paper we use data from 5 fields observed as part of the ACS GTO program. The total area is over 8 times the HDFN. These fields were selected to observe very nearby ( $z < 0.03$ ) galaxies or very distant ( $z > 4$ ) galaxies, so galaxies in the redshift range  $0.5 < z < 1.0$  should be representative of the universe at that redshift. The fields are in various parts of the sky, sampling a large volume in each redshift range ( $\sim 1.6 \times 10^4$  Mpc<sup>3</sup>  $0.5 < z < 0.75$  and  $\sim 2.4 \times 10^4$  Mpc<sup>3</sup>  $0.75 < z < 1.0$ ) so the effects of cosmic variance should be much smaller than in the Hub-

ble Deep Fields. In fact, the relative independence of our fields makes this survey more competitive with larger surveys than one might think based upon the areal coverage alone. We express all magnitudes in the AB system and use a  $\Omega_M = 0.3$ ,  $\Lambda = 0.7$  cosmology with  $H_0 = 70 \text{ km s}^{-1} \text{ Mpc}^{-1}$ . We define  $h_{0.7} = H_0/70$ .

## 2. DATA

The data were extracted from 5 fields observed by the ACS Wide Field Camera (WFC) between April 2002 and June 2003. The fields were selected to give accurate photometric redshifts (3 or more filters), to not have any primary targets in the range  $0.5 < z < 1.0$  and to not contain any clusters at lower redshifts. While the Hubble Deep Field North (HDFN) was only imaged in two ACS bands (F775W and F850LP), it has been imaged extensively in 7 optical and near infrared bands and has a large amount of spectroscopic follow-up. The combined area of these fields is  $47.9 \square'$ , over 8 times the area of the Hubble Deep Field North. The extinction values,  $E(B-V)$ , are taken from the Schlegel, Finkbeiner & Davis (1998) dust maps, and the total extinction in each filter,  $A(\text{filter})$ , is calculated using the method described in Schlegel, Finkbeiner & Davis (1998). A summary of the data properties in each field is given in Table 1 which lists the ACS filters, field-of-view, I-band exposure time,  $E(B-V)$ , I-band extinction, I-band zeropoint and the number of E/S0 galaxies in our sample.

### 2.1. NGC 4676

NGC 4676 is a low redshift pair of merging spiral galaxies and was observed as part of the ACS ‘‘Early Release Observations’’ (ERO) program (Ford et al. 2002). We mask out NGC 4676 and use galaxies in the background field. It was observed for 6740s in the F475W (g) filter, 4000s in the F606W (V) filter and 4070s in the F814W (I) filter. The area remaining after masking out the two prominent foreground galaxies is  $7.8 \square'$ .

### 2.2. UGC 10214

UGC 10214 is a low redshift spiral galaxy that is merging with a much smaller dwarf galaxy and has an extended tidal tail as a result (Tran et al. 2003). As with NGC 4676 it was selected as part of the ERO program. We mask out UGC 10214 and use galaxies in the background field (see Benítez et al. 2004). It was observed in 2 separate pointings giving a combined exposure of 13600s in F475W (g), 8040s in F606W (V) and 8180s in F814W (I). The area remaining after masking out the prominent foreground galaxy is  $10.7 \square'$ .

### 2.3. TN1338

TN J1338 –1942 (TN1338) is a radio galaxy at  $z = 4.1$  that was observed as part of our ACS/GTO program to study proto-clusters around high-redshift radio galaxies (see Miley et al. 2004, Overzier et al., in prep). It was observed for 9400s in F475W (g), 9400s in F625W (r), 11700s in F775W (i) and 11800s in F850LP (z). The total observed area is  $11.7 \square'$ .

### 2.4. TN0924

TN J0924 –2201 (TN0924), a radio galaxy at  $z = 5.2$ , was also observed as part of the high-redshift radio galaxy proto-cluster program (Overzier et al., in prep). It was observed for 9400s in F606W (V), 11800s in F775W (i) and 11800s in F850LP (z). The total observed area is  $11.7 \square'$ .

## 2.5. HDFN

The Hubble Deep Field North (HDFN) was observed with the ACS to find supernovae and test the ACS Grism (Blakeslee et al. 2003a). It was observed for 5600s in the F775W (i) filter and 10300s in the F850LP (z) filter. We use the ACS i-band for measurements of the structural parameters, but we do not have enough ACS filters for accurate photometric redshifts. However there is a deep 7-filter data available for the portion of the ACS image already observed by WFPC2 (Williams et al. 1996). We use the photometric catalog from Fernández-Soto, Lanzetta & Yahil (1999, FLY99), which has very deep F300W (U), F450W (B), F606W (V), F814W (I) WFPC2 and Kitt Peak National Observatory (KPNO) J,H,K band photometry. There are 146 spectroscopic redshifts from Cohen et al. (2000). We only use ACS data coincident with the deep WFPC2 image and take our photometric redshifts and colors from the FLY99 data. The observed area is  $5.8 \square'$ .

## 2.6. Catalogs

Each set of images was run through the ACS Science Data Analysis Pipeline (Blakeslee et al. 2003b). The data in each field were selected from the detection images produced from combining the filter images, weighted by the inverse noise squared. This aids in the detection of extremely faint objects by combining the signal from the different filters to produce a more significant detection. Source Extractor (Bertin & Arnouts 1996) was run first on the detection image and then in dual mode on the detection image and each filter image, to produce catalogs of the same objects, with photometry in matched apertures. We use these source catalogs as the starting point for selecting our sample and measuring the photometric properties.

## 3. MEASUREMENTS

### 3.1. Photometric Redshifts

We use the Bayesian Photometric Redshift code (BPZ, Benítez 2000) to calculate the photometric redshifts of galaxies in the fields of NGC 4676, UGC 10214, TN1338 and TN0924. This takes advantage of both the color information and a magnitude prior to constrain the redshift. The magnitude prior distinguishes nearby red galaxies (e.g. giant ellipticals) from distant, redshifted blue galaxies, which while having similar colors when seen through a small set of filters, will have very different magnitudes. We use the template spectra described in Benítez et al. (2004), which are based upon a subset of the templates from Coleman, Wu & Weedman (1980) and Kinney et al. (1996). The template set is: ‘El’, ‘Sbc’, ‘Scd’, ‘Im’, ‘SB3’ and ‘SB2’. These represent the typical spectral energy distributions (SED) of elliptical, early/intermediate type spiral, late type spiral, irregular and two types of starburst galaxies. These templates have been modeled using Chebyshev polynomials to remove differences between the predicted

colors and those of real galaxies. The final “calibrated” templates have been found to give better BPZ results on the HDFN (Benítez et al. 2004). We use extinction-corrected isophotal magnitudes to maximize the signal-to-noise on the color input to BPZ. In each case, the aperture is the same for each filter. The magnitude prior is based on the Hubble Deep Field North database (Williams et al. 1996) which uses deep ( $\sim 27$  mag arcsec $^{-2}$ ) isophotal magnitudes.

### 3.2. Testing BPZ

To test our photometric redshift catalogs for completeness, contamination, and systematic and random errors we compare them to spectroscopic data in the HDFN and to simulations. Fig. 1 shows the spectral energy distribution of an elliptical galaxy against the throughput of the filters used. The lower panel shows the HDFN filter set, consisting of the UBV $I$  WFPC2 filters and the JHK KPNO filters. The ‘El’ SED is plotted 3 times, at  $z = 0.5$  (dotted line), at  $z = 0.75$  (short dashed line), and at  $z = 1.0$  (long dashed line). The main feature of this spectrum is the 4000Å break, which is indicated by the bold arrow at each of these redshifts. The 4000 Å break is prominent in galaxies where there is very little ultraviolet radiation produced by hot, young stars, compared to the optical flux produced by an older stellar population. This break falls within the V or I filters at every redshift in the range that we use. The drop in flux per wavelength from one side of the break to the other side produces a significant change in magnitude from one filter to the next, leading to an accurate measurement of the photometric redshift.

The lower-middle panel shows the same plot for the ACS g, V and I filters used in the UGC10214 and NGC4676 fields. The upper-middle panel shows the g,r,i and z filters used in the TN1338 field. The top panel shows the V,i and z filters used in the TN0924 field.

We use the HDFN photometric and spectroscopic redshifts to estimate the errors for 3-color BPZ measurements of real galaxies seen through the WFPC2 filters and then use simulations to determine any biases in the BPZ measurements through ACS filters at the noise limits of our data. The g, V and I filters used in the UGC10214 and NGC4676 fields are similar in wavelength coverage to the B, V and I filters used in the HDFN dataset. Therefore we can test the accuracy of the photometric redshifts in these fields by calculating 3-color photometric redshifts for ellipticals in the HDFN. In the upper panel of Fig. 2, we plot the 3-color photometric redshifts calculated using the B, V and I filters against the 7 color photometric redshifts. The offset,  $\frac{z_{3BPZ} - z_{7BPZ}}{1 + z_{7BPZ}} = 0.010 \pm 0.074$ , is low and there are no outliers. We calibrate the 7-color photometric redshift to the spectroscopic sample and find a deviation  $\frac{z_{7BPZ} - z_{spec}}{1 + z_{spec}} = -0.045 \pm 0.026$ , shown in the middle panel of Fig. 2. There is one outlier, a galaxy with  $z_{BPZ} = 0.87$  and  $z_{spec} = 0.67$ . As expected from the poor fit, this object has  $(V - I)$  colors which are much redder and  $(B - V)$  colors which are slightly bluer than one would expect for an elliptical galaxy at this redshift. The bottom panel shows the 3-color photometric redshifts corrected for this offset. The correction is described at the end of this section. The quoted error in the above cases and for future BPZ measurements is for a single galaxy, so this offset is

significant. Cohen et al. (2000) show that the errors in the spectroscopic data are  $\Delta v = 200$  km s $^{-1}$ , implying  $\Delta z = 0.0007$ . The final error is consistent with the typical scatter found in the overall analysis of all HDF redshifts ( $\Delta z / (1 + z) = 0.06$ ). The offset between BPZ and spectroscopic redshifts, implies some evolution in elliptical galaxies from  $z = 0.2$  (the redshift of the calibration cluster) and  $z \sim 0.75$ .

Given that all of the HDFN ellipticals have good 3-band photometric redshifts, we expect that ellipticals in NGC4676 and UGC10214 should also have good photometric redshifts. However, the noise in these fields are somewhat greater than the HDFN, so there may be some missing objects.

We test the reliability of BPZ in each of the fields using Bouwens’ Universe Construction Set (BUCS, Bouwens, Magee & Illingworth, in preparation; Bouwens, Broadhurst & Illingworth 2003; Bouwens et al. 2004) simulations of  $r^{1/4}$  elliptical galaxies with three different SEDs: ‘El’, ‘Sbc’ and ‘Scd’ (Benítez et al. 2004). These simulations are designed to have the same noise characteristics as the observed ACS datasets and are processed in the same way as the data (§ 2.6). Therefore, the UGC 10214 simulation, with double the exposure time, has  $1.4\times$  the signal-to-noise of the NGC 4676 simulation. We use the 3 SEDs to test the reliability of redshifts for early-type galaxies with a range of colors. All the simulations are made up of galaxies with elliptical morphologies ( $\beta = 4$ ) and a Schechter luminosity function with parameters  $\phi^* = 0.00475$ ,  $M^* = -20.87$  and  $\alpha = -0.48$ . The density of galaxies was increased by a factor of 5 over the normal elliptical galaxy density to give a large sample of galaxies at each redshift. In these simulations elliptical galaxies are placed at random in 4 fields, each  $2000 \times 2000$  pixels. Each of these fields is approximately the area of a single amplifier on the Wide Field Camera.

Once the images had been processed we compared the simulation input catalog and the catalog of detected objects. The results are shown in Fig. 3. In each of the fields we find small differences between the measured redshift and the input redshift. The only major differences occur in the NGC4676 and UGC 10214 simulations, in the  $z_{simulation} = 0.95$  bin. In both cases  $z_{detection}$  is over estimated. Fig. 1 shows that at this redshift, the 4000Å break is in the middle of the F814W filter with no redder filter to compare to. This is also the redshift range at which there is increased scatter in 3-band photometric redshifts in the HDFN, which had a similar combination of filters. The offsets are due to the increased scatter and are not a systematic effect. We find that the TN1338 simulation has a mean scatter  $\sigma_z = 0.023$ , TN0924 has  $\sigma_z = 0.028$ , NGC 4676 has  $\sigma_z = 0.045$  and UGC 10214 has  $\sigma_z = 0.046$ . Since the HDFN has similar filters to NGC 4676 and UGC10214 and is deeper, we would expect  $\sigma_z$  to be lower. The additional noise is due to the real galaxy spectral energy distributions varying from the ideal templates used in our simulations. There is a large increase in the scatter for all galaxy types in the HDFN, UGC 10214 and NGC 4676 fields at  $z > 0.85$ , with the rms in the HDFN increasing from  $\sigma_z = 0.029$  ( $z < 0.85$ ) to  $\sigma_z = 0.068$  ( $z > 0.85$ ) and the rms in the UGC 10214 and NGC 4676 fields increasing from  $\sigma_z = 0.036$  ( $z < 0.85$ ) to  $\sigma_z = 0.050$  ( $z > 0.85$ ).

We can use the simulations to check for incompleteness. All of the galaxies with  $B_{z=0} \leq 24.5$  mag ( $B_{z=0} \leq 24.0$  mag at  $z > 0.75$ ) were detected apart from one or two galaxies close to the edge of each image, one or two with a nearby neighbor or a few galaxies at  $z > 1.2$  in TN0924. At fainter magnitudes the errors become very large for galaxies in NGC4676 in particular. Altogether 15% of  $0.5 < z < 1.0$  objects have  $-0.06 < \Delta z / (1+z) > 0.06$  and only 6% have  $-0.12 < \Delta z / (1+z) > 0.12$ . There is also around 2% contamination from lower or higher redshifts ( $z < 0.3$  and  $z > 1.2$ ).

We correct the BPZ redshift estimates to account for the difference between the spectroscopic and BPZ measurements for elliptical galaxies:

$$z_{\text{best}} = \frac{z_{\text{BPZ}} + 0.045}{(1 - 0.045)} \quad (1)$$

$z_{\text{best}}$  is plotted against  $z_{\text{spec}}$  in the lower panel of Fig. 2.

This changes the input BPZ redshift range to  $0.43 < z_{\text{BPZ}} < 0.91$ . It also reduces the errors associated with  $z_{\text{BPZ}} > 0.85$  galaxies in UGC 10214 and NGC 4676 considerably. We use the Benítez et al. (2004) errors ( $\sigma_z = 0.06$ ) for our BPZ measurements. We find that a few (7) of our objects have significantly broader probability density functions. The width of these PDFs are added in quadrature to the initial  $\sigma_z = 0.06$ . The objects in UGC 10214 and NGC 4676 with  $z_{\text{BPZ}} > 0.85$  are given an uncertainty  $\sigma_z = 0.09$ . This takes into account both template error (errors related to mismatches between the real and assumed templates) and random errors (due to the noise).

In summary, our final sample contains 72 galaxies, 10 of which have spectroscopic redshifts. The completeness is expected to be in excess of 95% ( $\lesssim 3$ -4 missing galaxies), with a contamination of less than 2-3 galaxies (from redshift uncertainties). We list the properties of all our galaxies in Table 2, in two redshift intervals ( $0.5 < z \leq 0.75$ ,  $0.75 < z \leq 1.0$ ). Within each interval they are listed in order of increasing restframe  $(U - V)_0$  color (see Section 5.1).

### 3.3. Measuring the Half-light Radius and Total Magnitude

We calculate the half-light radius  $r_e$  of each galaxy using GALFIT (Peng et al. 2002). In each case we assume a single Sersic profile (see Eqn. 2) and allow the Sersic parameter ( $\beta$ ) to vary between 0 and 10.

$$I(r) = I_{r_e} \exp \left\{ -k \left[ \left( \frac{r}{r_e} \right)^\beta - 1 \right] \right\} \quad (2)$$

where  $I_{r_e}$  is the surface brightness at the half-light radius,  $r_e$ , and  $k \sim 1.9992\beta - 0.3271$  (Capaccioli et al. 1989). The half-light radius is defined along semi-major axis. Since the shape and size of the galaxy can be strongly affected by the background, we force the sky to the value calculated by Source Extractor.

An alternative way of measuring the half-light radius is through the growth curve. The growth curve analysis uses a maximum likelihood fit to the measured flux in 14 circular apertures to estimate the Sersic parameter and

half-light radius. We find that the correction from circular half-light radius to elliptical half-light radius is well fit by a Moffat profile,  $r_e^{\text{ell}} = r_e^{\text{cir}} (1 + (\frac{1}{a})^2)^b / (1 + (\frac{\phi}{a})^2)^b$ , where the  $\phi$  is the ratio of semiminor axis to semimajor axis and the Moffat parameters  $a$  and  $b$  are only weakly dependent on the Sersic profile. The best fit parameters for an exponential profile ( $\beta = 1$ ) are  $a = 0.38$  and  $b = 0.28$ , whereas a de Vaucouleur's profile ( $\beta = 4$ ) is well fit by  $a = 0.24$  and  $b = 0.21$ . Therefore, if  $\phi = 0.8$ ,  $\frac{r_e^{\text{ell}}}{r_e^{\text{cir}}} = 1.11$  and  $\frac{r_e^{\text{ell}}}{r_e^{\text{cir}}} = 1.09$  for  $\beta = 1$  and  $\beta = 4$  respectively, and if  $\phi = 0.6$ ,  $\frac{r_e^{\text{ell}}}{r_e^{\text{cir}}} = 1.26$  and  $\frac{r_e^{\text{ell}}}{r_e^{\text{cir}}} = 1.22$  respectively. These two examples demonstrate the weak dependency on  $\beta$ . Once the best fit parameters are found, a new total flux is calculated and the process is iterated until the new flux is no longer larger than the old flux.

We use the output from GALFIT for the rest of our analysis since it is corrected for the PSF, which is important for galaxies with  $r_e < 0.4''$ , but use the growth curve to identify outliers. The scatter in the two measurements is linear with size:

$$\Delta r_e = 0.25 r_e - 0.013 \quad (3)$$

Outliers are objects where the difference between the growth curve and GALFIT is greater than 2.0 times the standard error at that size. The few outliers found had nearby neighbors that affected the growth curve analysis or GALFIT. In each case the size was checked manually. In most cases GALFIT gave the best fit, but for the largest object (number 30, in Table 2), we found that neither the growth curve or GALFIT yielded a good fit. We used the ELLIPROF task in Vista to get an ellipse fit model and IRAF PHOT procedure to continue the growth curve out to larger apertures. Both methods give an elliptical half light radius  $r_e = 1.75''$  compared to  $r_e = 1.34''$  for the original growth curve method and  $r_e = 2.05''$  for GALFIT. Once we got our best fit half-light radius, we ran GALFIT with this fixed half-light radius to get the Sersic parameter and total magnitude.

We convert the apparent half-light radius (in arcsec) to the intrinsic half-light radius (in kpc) using:

$$R_e = 4.85 \times 10^{-3} r_e d_a(z, \Omega_m, \Lambda, H_0) \quad (4)$$

where  $d_a$  is the angular-size distance (in Mpc) calculated from the redshift and cosmology.

### 3.4. The Rest-frame B-band magnitude.

The rest-frame Johnson B band has a mean wavelength  $\sim 4400\text{\AA}$  which translates to  $\sim 7700\text{\AA}$  at  $z = 0.75$ . This puts it into either the F775W-band or F814W-band, available for our datasets. Most of the rest-frame B flux falls within these bands, so the k-corrections from these bands should be the smallest and most accurate, and similarly for the structural parameters. For convenience, we let the I-band refer to either F775W or F814W throughout this section. Converting from these filters to the  $z = 0$  Johnson B removes any differences particular to the passband. Correcting to total magnitudes removes any differences particular to the depth. Once these corrections have been made the data from all fields should be homogeneous and

the only differences should come from cosmic variance and the field-of-view.

The rest-frame B-band magnitude is calculated using the k-correction of the best fit BPZ SED from the I band to the  $z=0$  Johnson B-band.

$$B_{z=0,iso} = I_{iso} + k(\text{SED}, I, z_{\text{BPZ}}, B, 0) \quad (5)$$

where the k-correction  $k(\text{SED}, I, z_{\text{BPZ}}, B, 0)$  is the difference in magnitude between the integrated flux through an I-band filter at  $z_{\text{BPZ}}$  and the B-band filter at  $z = 0$ . The SEDs fit our colors best at  $z_{\text{BPZ}}$  rather than  $z_{\text{best}}$ , so we must use the  $z_{\text{BPZ}}$  to calculate the k-correction.  $B_{z=0,iso}$  and  $I_{iso}$  are the restframe B band and measured I band isophotal magnitudes, which have a strong dependence on the surface brightness limit and the redshift (Cross et al. 2001), so a correction must be made for the missing flux. GALFIT calculates the total flux of each galaxy in the I-band, which we then trivially convert to a total I-band magnitude  $I_T$ . We can transform this to the total rest-frame B magnitude,  $B_{z=0,T}$ .

$$B_{z=0,T} = B_{z=0,iso} + I_T - I_{iso} \quad (6)$$

The total magnitude is between 0.1 and 0.7 mag brighter than the isophotal magnitude, with a mean aperture correction of 0.34 mag. Finally we convert to absolute magnitudes. Since we have already k-corrected and extinction corrected the data, the equation is simply:

$$M_{B,T,z=0} = B_{z=0,T} - 5 \log(d_L) - 25. \quad (7)$$

where the luminosity distance  $d_L$  is in Mpc. The effective surface brightness of the galaxy is defined as the mean surface brightness within the half-light radius. The intrinsic effective surface brightness is calculated from the absolute magnitude and half-light radius to remove the  $(1+z)^4$  redshift dependence:

$$\mu_e = M_B + 5 \log_{10} R_e + 38.57 \quad (8)$$

where the constant converts from magnitudes per kpc to mag arcsec<sup>-2</sup>.

#### 4. SAMPLE SELECTION

We select elliptical and S0 (E/S0) galaxies on the basis of morphology to a rest-frame B magnitude limit that gives us the largest sample with reliable redshifts and morphologies. We select over a redshift range  $0.5 < z_{\text{best}} < 1.0$  since the 4000 Å break is outside our range of filters for  $z < 0.25$  and  $z > 1.25$ . For redshifts close to these limits it will be increasingly difficult to estimate an accurate photometric redshift. The k-corrections between I-band and rest-frame B-band have a very weak dependence on the SED across this range and have the weakest dependence at  $z = 0.75$ . At  $z < 0.5$ , the errors in the k-correction increase (the standard deviation across the range of SEDs is 0.16 mag at  $z = 0.5$  and 0.28 mag at  $z = 0.3$ ), and the additional volume over which galaxies can be seen is relatively small. For  $z > 1.0$ , the errors in the k-corrections increase, and the range of absolute magnitudes that can be sampled decreases. At  $z = 1$ , it is possible to see  $M_B < -20.1$  galaxies, by  $z = 1.2$ , the combination of distance modulus and

k-correction reduces the range to  $M_B < -21.6$ , so only the very brightest galaxies  $\sim M_B^*$  will be sampled.

Initially, galaxies are selected with  $0.5 \leq z < 1.0$  and  $B_{z=0,iso} \leq 25.5$  mag. Stars are removed by selecting and removing objects with the SExtractor stellarity flag  $> 0.8$ . This sample was morphologically classified using a semi-automated method. The first part of the classification was by eye. For an object to be selected as an early-type galaxy, it had to be axi-symmetrical, centrally concentrated and must not have any spiral features. This removes spiral galaxies, chain galaxies, mergers, irregulars and most starbursts. The galaxies that were selected as early types were then run through GALFIT as described above to determine the half-light radius, Sersic parameter and total magnitude. Objects with  $\beta < 2$  or  $r_e < 0.1$  were removed from the sample. The  $\beta \gtrsim 2$  criterion is effective at removing any residual irregular or starburst galaxies which were not caught by the first test. Removing  $r_e < 0.1$  galaxies, eliminates those objects where the errors on  $r_e$  and  $\beta$  will be large, dominated by the seeing and pixel scale. These objects may not really be E/S0 galaxies, even if we measure  $\beta > 2$ . We find that morphological classification is easy for  $I < 24$  mag, but becomes progressively more difficult at fainter magnitudes until it becomes almost impossible at  $I > 25$  mag.

Since we are interested in the rest-frame B-band properties of our galaxies, our magnitude limit should be the total rest-frame B magnitude. The main criterion for sample selection is the magnitude at which photometric redshifts and morphological classification become unreliable.

Fig. 5 shows the difference between the total rest-frame  $B_{z=0,T}$  magnitude and the  $I_{iso}$  magnitude. For  $z < 0.75$ , there is a fairly constant offset  $B_{z=0,T} - I_{iso} = 0.61$  mag with a scatter of 0.2 mag, and the offset for  $z \geq 0.75$  is  $B_{z=0,T} - I_{iso} = 0.17$  mag with a scatter of 0.3 mag. Using a limit  $B_{z=0,T} = 24.5$  mag at  $z < 0.75$  is equivalent to a limit of  $I_{iso} = 23.89$  and  $B_{z=0,T} = 24.0$  mag at  $z > 0.75$  is equivalent to a limit of  $I_{iso} = 23.83$ .

The data can be used to test these limits, using the odds value that is calculated in BPZ. The odds value is the integration of the probability density function (PDF) between 2 standard deviations of the Bayesian redshift.

$$\text{Odds} = \int_{z_{\text{BPZ}} - 2\sigma}^{z_{\text{BPZ}} + 2\sigma} \text{pdf}(z) dz \quad (9)$$

Benítez et al. (2004, in preparation) determined the standard deviation to be  $\sigma = (1+z)\sigma_z$  where  $\sigma_z = 0.06$ . Thus a galaxy with a well-defined PDF, a single peak with a small standard deviation should have an odds value  $\geq 0.95$ . 75% of galaxies of  $z_{\text{best}} \leq 0.75$  and 85% of  $z_{\text{best}} > 0.75$  have odds  $\geq 0.95$ . If the magnitude limits are increased by 0.5 mag, only 67% of the new  $0.5 \leq z < 0.75$  galaxies have odds  $\geq 0.95$  and only 33% of the new  $0.75 \leq z < 1.0$  have odds  $\geq 0.95$ . Both the BPZ results from the simulations and the data suggest the best limits are  $B_{z=0,T} < 24.5$  for  $z < 0.75$  and  $B_{z=0,T} < 24.0$  for  $z \geq 0.75$ , both roughly equivalent to  $I_{iso} < 24.0$ .

In summary, the final selection criteria are: Morphologically elliptical galaxies, defined by a centrally-concentrated, axisymmetric profile with  $r_e \geq 0.1''$  and  $\beta \geq 2$ . Objects in our lower redshift sample  $0.5 < z < 0.75$  have a rest-frame B-band magnitude limit of 24.5 mag

(observed  $I \lesssim 23.5$ ) while objects in our higher redshift sample  $0.75 < z_{\text{best}} \leq 1.0$  have a  $B$ -band magnitude limit of 24.0 mag (observed  $I \lesssim 23.5$ )

The  $0.5 \leq z < 0.75$  sample contains 32 galaxies and the  $0.75 \leq z < 1.0$  sample contains 40 galaxies. Since our samples are morphologically selected rather than color or SED selected we will be able to study the color evolution of the galaxies. In Fig. 6 we show all of the galaxies in our data set. These are ordered in the same way as Table 2.

#### 4.1. Errors

The final redshift errors are calculated from the BPZ of Benítez et al. (2004). This gives  $\Delta z = 0.06(1+z)$  as the final photometric redshift errors that we use. The errors in the spectroscopic redshifts are  $\Delta z = 0.0007$  from Cohen et al. (2000). The error bars in absolute magnitude, half-light radius and surface brightness are calculated from the errors in magnitude, half-light radius and redshift:

$$\Delta M_B = \sqrt{(\Delta B)^2 + \left(\frac{\partial M}{\partial z} \Delta z\right)^2} \quad (10)$$

$$\Delta R_e = R_e \sqrt{\left(\frac{\Delta r_e}{r_e}\right)^2 + \left(\frac{\partial d_a}{\partial z} \Delta z\right)^2} \quad (11)$$

$$\Delta \mu_e = \sqrt{(\Delta B)^2 + \left(\frac{4.3 \Delta z}{(1+z)}\right)^2 + \left(\frac{2.2 \Delta r_e}{r_e}\right)^2} \quad (12)$$

where  $\Delta B$  is the final error in the restframe B-band magnitude. This includes the measured error in the F775W or F814W magnitude calculated in the ACS pipeline, which ranges from  $\Delta m = 0.002$  mag to  $\Delta m = 0.08$  mag, the error in the k-correction from the F775W/F814W to rest-frame B ( $\Delta k \sim 0.05$  mag), the uncertainty in the zeropoint ( $\Delta zp \sim 0.02$  mag) and the uncertainty in the isophotal to total magnitude correction ( $\Delta m_{\text{tot}} \sim 0.05$  mag). For objects with photometric redshifts, the errors are dominated by the redshift error.

## 5. PROPERTIES OF EARLY TYPE GALAXIES

### 5.1. Colors of Early Type Galaxies

An unbiased look at the colors of E/S0 galaxies is important, not only for understanding their star formation history, but also for understanding the role that color selection has in isolating large samples of these objects at high redshift. Such color (or SED) selections have already been employed in the CFRS, CADIS, and COMBO-17 surveys and are relatively cheap to perform, requiring only ground-based imaging over large areas of the sky. Morphologies and structural properties are, by contrast, much more expensive to acquire, requiring the unique high resolution capabilities of HST. But, the cheaper route may not be the best route as selecting by color can result in contamination from particularly red later types (non-E/S0s) or incompleteness to blue E/S0s.

Fig. 7 plots the absolute B-band magnitude against the rest-frame  $(U - V)_{z=0}$  (AB) color. This is calculated in the same way as the rest-frame B magnitude:

$$(U - V)_{z=0} = [m_{F1} + k(\text{SED}, F1, z_{\text{BPZ}}, U, 0)] - [m_{F2} + k(\text{SED}, F2, z_{\text{BPZ}}, V, 0)] \quad (13)$$

where  $m_{F1}$  and  $m_{F2}$  are the magnitudes in the closest filters (Filter1 and Filter2) to the redshifted rest-frame  $U$  and  $V$  filters. Filter1 and Filter2 are defined in Table 3 for each field. The SED is the best-fit SED (or linear combination of SEDs) from BPZ and  $k(\text{SED}, m_{F1}, z_{\text{BPZ}}, U, 0)$  is the k-correction between the observed filter at  $z_{\text{BPZ}}$  and the Johnson U band filter at  $z = 0$ .

We find a significant range in colors of early-type galaxies, with the majority having  $(U - V)_0 > 1.7$ . Those with  $(U - V)_0 > 1.9$  have colors similar to the classic red ellipticals that form the red sequence seen in both clusters (Blakeslee et al. 2003c) and the field (Bell et al. 2004). The red colors are consistent with an old coeval population of stars. While there is a slight color magnitude relationship for  $(U - V)_0 > 1.9$  galaxies, the red sequence is blurred by a combination of the wide redshift range and errors in the photometric redshift. For the remainder of the paper we define galaxies with  $(U - V)_0 > 1.7$  as ‘red’ and galaxies with  $(U - V)_0 < 1.7$  as ‘blue’.

There is a set of early-type galaxies with  $(U - V)_0 < 1.7$ . These have a broad color distribution, implying a wide range in age or metallicity, with some ongoing star-formation. There is also a wide range in absolute magnitude for  $(U - V)_0 > 1.1$ ,  $-22.5 < M_B < -18$ . The lower panel of Fig. 8 shows the reliability of the redshift with color.

The redshift odds are good for more than 80% of the galaxies with a small dependence on color (see §4, Eqn 9). The fraction of galaxies with just a single peak or a narrow dominant peak (total probability greater than 90%) in the probability density function is shown by the solid histogram in the middle panel of Fig. 8. The fraction is  $> 85\%$  for all but the bluest,  $(U - V)_0 < 1.12$ , galaxies where it is reduced to  $\sim 60\%$ . Some of these galaxies have a slightly wider probability density function with a few nearby peaks that overlap. These can be used, but have a large uncertainty in their photometric redshifts. We also have two galaxies with a secondary peak at  $z \sim 4$ . In the top panel of Fig. 8 we show the uncertainty as determined from the PDF. The open squares denote the galaxies with a dominant narrow peak and the filled squares represent those with overlapping peaks. The filled circles are the mean uncertainty calculated in the simulations for the 3 different SEDs. Galaxies with  $1.4 < (U - V)_0 < 1.9$  have the lowest uncertainties and the greatest chance of having a single peaked probability distribution function. Bluer galaxies have larger uncertainties and greater chance of a multi-peaked distribution. We take into account the increased uncertainty resulting from the broader probability distributions.

We will use the  $(U - V)_0$  colors calculated here to test the effect of color selection on the luminosity function and structural properties, but note that one color by itself is not enough to put constraints on both the age and star-formation timescale of these galaxies.

To estimate the ages of galaxies, we use the methodology of Menanteau, Abraham & Ellis (2001) to fit exponentially decaying starburst models to the colors of early type galaxies. But instead of fitting to the radial variations in color, we use a simpler method, fitting to the overall colors. We use the Bruzual & Charlot (2003) models to calculate the

expected colors for a set of exponentially decaying continuous starburst models. These models assume a Salpeter Initial Mass Function and solar metallicity. The time scales for the exponential decay ( $\tau$ ) were allowed to have the following values: 0.1, 0.2, 0.4, 1.0, 2.0, 5.0, 9.0 Gyr. Elliptical galaxies are generally expected to have very short timescales ( $\tau \leq 1$  Gyr), while late-type galaxies are expected to have much longer timescales ( $\tau > 2$  Gyr). The models calculate the expected magnitudes in each filter at a given redshift for a variety of galaxy ages ( $T$ ). For each field we produced the models for redshifts from 0.4 to 1.1 at intervals of 0.05.

Using the set of models where the redshift most closely matches our redshift estimate  $z_{\text{best}}$  for each object, the model colors were compared to the measured colors, after converting from Vega to AB magnitudes. We calculated the maximum likelihood for the different values of  $\tau$  and ( $T$ ) using the following equation:

$$\ln \mathcal{L} = \sum_i \left[ \ln(2\pi\sigma_{C,i}^2) + \left( \frac{C_{\text{mod},i}(\tau, T) - C_i}{\sigma_{C,i}} \right)^2 \right] + \ln(p) \quad (14)$$

where  $C_i$  are the measured colors (e.g. [g-V] and [V-I] in the case of NGC4676),  $\sigma_{C,i}$  are the errors in the measured colors and  $C_{\text{mod},i}(\tau, T)$  are the model colors, a function of the timescale  $\tau$  and the age  $T$ . A prior  $p$  is used such that the combination of age and lookback-time does not exceed the age of the universe in the adopted cosmology.

$$\begin{aligned} p &= 1; t_{\text{frm}} < T_{\text{uni}} - 1.0 \text{ Gyr} \\ &= \frac{(T_{\text{uni}} - t_{\text{frm}} - 0.5 \text{ Gyr})}{(0.5 \text{ Gyr})}; 0.5 \text{ Gyr} < T_{\text{uni}} - t_{\text{frm}} < 1.0 \text{ Gyr} \\ &= 0; t_{\text{frm}} > T_{\text{uni}} - 0.5 \text{ Gyr} \end{aligned} \quad (15)$$

where  $t_{\text{frm}} = T + t[z, (\Omega_M, \Lambda, H_0)]$  is the formation time of the galaxy and  $T_{\text{uni}} = 13.5$  Gyr is the age of the universe in the adopted cosmology.

We used the following combinations of adjacent filters for each field. UGC10214 / NGC4676: ( $g - V$ ), ( $V - I$ ); TN0924: ( $V - i$ ), ( $i - z$ ); TN1338: ( $g - r$ ), ( $r - i$ ), ( $i - z$ ); HDFN: ( $U - B$ ), ( $B - V$ ), ( $V - I$ ). In Fig. 9 we plot the star formation timescale ( $\tau$ ) against the galaxy age (bottom left hand panel), against the lookback time (bottom middle hand panel) and formation time (bottom right hand panel) as square points (both open and filled). The top panels show the histogram of galaxy age, lookback time and formation time. The error bars are calculated using a Monte Carlo simulation assuming Gaussian errors in the redshift and colors.

Most galaxies have  $\tau \leq 1$  Gyr suggesting an intense period of star formation that then rapidly decreased. We see a strong peak in galaxy ages of 2 Gyrs, but a wide spread with  $T < 1$  Gyr and  $T > 7$  Gyr in some cases. The formation times show a peak at  $1.5 < z < 2$  ( $8.5 < t_{\text{frm}} < 10$  Gyr), consistent with the star formation history seen in Heavens et al. (2004), with a rapid falloff at high redshift and a lower limit at the lookback time of our sample.

Fig. 7 also shows the expected evolutionary tracks of galaxies with different masses and decay timescales. Galaxies undergoing pure luminosity evolution with an

exponentially decaying star-formation rate as described above will move along these tracks from blue to red. The tracks show that these galaxies, regardless of the decay timescale reach a maximum B-band luminosity at  $(U - V)_0 < 0.7$  and then they gradually fade as they redden. The Bruzual-Charlot models are calculated for a 1 stellar mass object, so the evolutionary tracks are calculated by scaling  $M_B^{z=0}$  by  $10^{11}$  and  $10^{12}$ . While most of the  $(U - V)_0 > 1.7$  E/S0s have  $M > 10^{11} M_\odot$  and some have  $M > 10^{12} M_\odot$ , the bluer E/S0s,  $1.2 < (U - V)_0 < 1.7$ , have  $10^{10} < M < 10^{11} M_\odot$  and those with  $(U - V)_0 < 1.2$  have only  $M < 10^{10} M_\odot$ . Note that these results should be treated with caution given their obvious dependence on our simple exponentially decaying model. The very brightest of the blue E/S0s will end up amongst the red sequence that has already formed, but most will end up extending the sequence to fainter absolute magnitudes, given pure luminosity evolution. For reference, the expected color of a ‘red’ elliptical at  $z = 0$  is  $(U - V)_0 = 2.18$  assuming the Coleman, Wu & Weedman (1980) SED, so even the reddest galaxies in the sample will undergo an additional 0.1 – 0.2 magnitudes of reddening to  $z = 0$ .

Galaxies at lower redshifts can be seen to fainter luminosities, so it is best to compare objects over a volume limited sample (i.e., where all objects are seen over the same absolute magnitude and intrinsic size ranges). The dashed histograms and filled points in Fig. 9 show galaxies with  $M_B < -20.1$  mag and  $R_e > 0.8$  kpc. The peak formation age is slightly higher at  $2 < z < 2.5$  ( $10 < t_{\text{frm}} < 11$  Gyr). This is consistent with the Heavens et al. (2004) results that show that more massive galaxies form earlier.

It is useful to compare the rest-frame  $(U - V)_0$  colors to the Bruzual & Charlot (2003) model results since these were calculated using very different methods. In Fig. 10 we plot  $(U - V)_0$  against the number of decay timescales ( $N_\tau = T/\tau$ ). As expected, there is a strong correlation between these numbers over the range  $1 < N_\tau < 10$ .

The strong correlation between the  $(U - V)_0$  color and the more complicated modeling that leads to age and decay timescale indicates that many past surveys for early-type galaxies (e.g., CFRS, COMBO-17 and CADIS) will preferentially miss the younger versions of these galaxies. For COMBO-17 and CADIS, the  $(U - V)_0 > 1.7$  selection eliminated objects that have undergone star-formation for less than 7 decay timescales, and for the CFRS, the  $(U - V)_0 > 1.38$  selection eliminated objects at less than 4 decay timescales.

Early-type galaxies must have gone through a period of high star-formation, and the youngest of these galaxies are being systematically missed by ground-based surveys that select by color or SED, rather than morphology.

Menanteau et al. (2004) looked at the color gradients of galaxies in the UGC10214 field and showed that 30 – 40% of field ellipticals are from  $0.3 < z < 1.2$  are blue and that the blue colors occur preferentially in the cores. We find that 39% of all our galaxies have  $(U - V)_0 < 1.7$  and 33% of our volume limited sample have  $(U - V)_0 < 1.7$ , in complete agreement. The Menanteau et al. (2004) results show that the ongoing star-formation is localized to the core.



When we look at the structural properties of galaxies it is important to understand the selection effects. Fig. 11 shows the distribution of galaxies in absolute magnitude and surface brightness, the Bivariate Brightness Distribution (BBD, Cross et al. 2001). Galaxies that are in the unshaded region meet the selection criteria (in magnitude, half-light radius and surface brightness) at all redshifts in the ranges prescribed. In this plot and most of the following plots, we use shading to highlight the visibility of galaxies. No shading is used when objects have the maximum visibility, i.e. they can be seen right across the redshift range. Cross-hatching is used when, given our selection criteria, no galaxies can be seen (visibility is zero). Light shading denotes parts of parameter space where a galaxy can be seen at the minimum redshift but not all the way to the maximum redshift. The visibility function shows us when a correlation is real or is due to a selection effect. It also helps us to properly weight our data.

The absolute selection limits are calculated from the apparent  $z$ ,  $r_e$ ,  $B_{z=0}$  and  $\mu_{lim}^{app}$  selection limits, using Eqns 4,7 and  $\mu_{lim} = \mu_{lim}^{app} - 10 \log_{10}(1+z)$ . The low surface brightness boundary is the limit at which the mean surface brightness of a galaxy within the half-light radius is lower than the threshold of the shallowest survey (i.e. NGC4676,  $\mu_{lim,I}^{app} = 25.2$  mag arcsec $^{-2}$ ) and so it becomes difficult to accurately measure the half-light radius. The following absolute selection limits are used:  $0.5 < z < 0.75$  range ( $z = 0.5$ ),  $M_B^{z=0} = -17.8$  mag,  $\mu_{lim,B} = 23.9$  mag arcsec $^{-2}$ ,  $R_e = 0.61$  kpc;  $0.5 < z < 0.75$  range ( $z = 0.75$ ),  $M_B^{z=0} = -18.8$  mag,  $\mu_{lim,B} = 23.3$  mag arcsec $^{-2}$ ,  $R_e = 0.73$  kpc;  $0.75 < z < 1.0$  range ( $z = 0.75$ ),  $M_B^{z=0} = -19.3$  mag,  $\mu_{lim,B} = 22.8$  mag arcsec $^{-2}$ ,  $R_e = 0.73$  kpc;  $0.75 < z < 1.0$  range ( $z = 1.0$ ),  $M_B^{z=0} = -20.1$  mag,  $\mu_{lim,B} = 22.2$  mag arcsec $^{-2}$ ,  $R_e = 0.80$  kpc.

The  $0.5 < z < 0.75$  sample has a narrow range in surface brightness ( $18.5 < \mu_e < 21$  mag arcsec $^{-2}$ ), with one outlier. This is the galaxy found earlier to have  $r_e = 1.75''$ , corresponding to  $R_e = 11.0$  kpc. The  $0.75 < z < 1.0$  sample has a wider range in surface brightness ( $17.5 < \mu_e < 21.5$  mag arcsec $^{-2}$ ).

In the unshaded region where galaxies can be seen over the whole range of redshifts, the volume over which a galaxy can be seen is constant, and so the space density is proportional to the number of galaxies. This 'volume-limited' sample is useful for comparing galaxies over a range of magnitudes. To compare galaxies within each redshift range, we use a sample that is volume-limited from  $0.5 < z \leq 1.0$ , with  $M_B \leq -20.1$  mag and  $R_e > 0.8$  kpc. Only 20 of the 32 galaxies from the  $0.5 < z < 0.75$  subsample makes it into this volume-limited sample, and 34 of the 40 galaxies in the  $0.75 < z < 1.0$  subsample (Table 2). The ratio of galaxies in these two samples is 1 : 1.7 (20:34), which is very similar to the ratio of comoving volume: 1 : 1.5.

In Fig. 12 we compare the histogram of the Sersic parameters in each redshift range. The lower panel shows the  $0.5 < z \leq 0.75$  sample and the upper panel shows the  $0.75 < z \leq 1.0$  sample. The long-dashed line represents the full distribution at each redshift and the solid line represents the equivalent volume limited samples, selected at  $M_B \leq -20.1$  mag and  $R_e \geq 0.8$  kpc. To compare each distribution we calculate the biweight and biweight-scale

(Beers, Flynn & Gebhardt 1990). These are equivalent to the mean and standard deviation in the case of a Gaussian distribution and a large number of data points. The biweight is more robust in the case of a non-Gaussian distribution with small-number statistics. The biweight and biweight-scale values of  $\beta$  in the volume limited sample are tabulated in Table 4, for both redshift ranges and for 'red' galaxies,  $(U-V) > 1.7$ , and 'blue' galaxies  $(U-V) < 1.7$ . The biweight,  $\langle \beta \rangle \sim 4.4$  for the present sample and does not vary significantly with redshift or color. The  $(U-V) > 1.7$  have slightly lower values, closer to the de Vaucouleur's value ( $\beta = 4.0$ ), and the bluer galaxies have larger values on average, although with a larger biweight-scale, indicating a wider range of values. The larger values of  $\beta$  are consistent with the bluer galaxies having a starburst in the cores: the central regions will be slightly brighter, making the galaxies appear more concentrated. However, at fainter luminosities  $-20.1 < M_B < -18.8$ , the distributions become significantly different. There is a significant increase in the number of low  $\beta$ , 'blue' galaxies, leading to a biweight of  $\langle \beta \rangle = 2.7$  compared to  $\langle \beta \rangle = 4.1$  for the 'red' galaxies. Kolmogorov-Smirnov tests demonstrate that the 'blue' and 'red' galaxies with  $M_B \leq -20.1$  mag and  $R_e \geq 0.8$  kpc are equivalent to each other at 85% and 55% confidence in the redshift ranges  $0.5 < z < 0.75$  and  $0.75 < z < 1.0$ , respectively. At fainter magnitudes ( $M_B \geq -18.8$  mag), this probability decreases to 1%, thus implying a split in the properties between 'red' and 'blue' early-type galaxies. This latter comparison is only possible in our lower redshift slice  $0.5 < z < 0.75$ , for objects with  $R_e \geq 0.73$  kpc.

Fig. 13 shows the histogram of half-light radii. The results for the volume limited sample are summarised in Table 4. The distribution of  $R_e$  appears uneven, considering the smooth distribution of  $\beta$ . Again there is no change between the two redshift ranges with the biweight size  $\sim 2.6$  kpc and there is no significant difference in the biweight sizes of red or blue early-types in either redshift range. The Kolmogorov-Smirnov test gives high probabilities 73% and 79% that the 'red' and 'blue' galaxies have equivalent size distributions with  $M_B \leq -20.1$  mag and  $R_e \geq 0.8$  kpc at  $z < 0.75$  and  $z \geq 0.75$ , respectively. At lower luminosities, the biweight size is lower, and the difference between the 'red' and 'blue' distributions is greater with a K-S probability of 52%. However the discrepancy is much lower than with the Sersic parameters.

Comparing samples in the same luminosity range can be misleading, since ellipticals are expected to show luminosity evolution simply as a result of passive evolution in the stars. Ideally one would like to compare objects of the same mass, but without dynamical information we compare the luminosity of objects of a similar size, since size is expected to change more slowly. Schade et al. (1999) looked at the relationship between half-light radius and B-band absolute magnitude of field ellipticals. They used 17 ellipticals in the range  $0.5 < z \leq 0.75$  (15 had spectroscopic redshifts) and 20 in the range  $0.75 < z \leq 1.0$  (11 had spectroscopic redshifts). We have a larger sample, which extends to fainter absolute magnitudes, but fewer spectroscopic redshifts (4 out of 32 and 6 out of 40, respectively, for our two subsamples). Schade et al. (1997) find that cluster ellipticals are

fit well by  $M_B = -3.33 \log(R_e) - 18.65 + \Delta M_B$  where  $\Delta M_B = s \log(1+z)$  and in Schade et al. (1999) they show that  $\Delta M_B = -0.56 \pm 0.3$  for ellipticals in the range  $0.5 < z \leq 0.75$  and  $\Delta M_B = -0.97 \pm 0.14$  for ellipticals in the range  $0.75 < z \leq 1.0$ . In Fig. 14 we measure the relationship between  $M$  and  $R_e$  for our galaxies. Schade et al. (1999) used a cosmology with  $\Omega_M = 1.0, \Lambda = 0$ . and  $H_0 = 50 \text{ km s}^{-1} \text{ Mpc}^{-1}$ . Converting to the cosmology used in this paper, we now have the relationship  $M_B = -3.33 \log(R_e) - 18.56 + \Delta M_B$  at  $0.5 < z \leq 0.75$  and  $M_B = -3.33 \log(R_e) - 18.60 + \Delta M_B$  at  $0.75 < z \leq 1.0$ . The results are tabulated in Table 4.

The solid lines in Fig. 14 show our best fit results for  $\Delta M_B$  in the volume limited sample (i.e the parameter space not shaded). We find  $\Delta M_B = -0.78 \pm 0.07$  ( $\chi_\nu^2 = 3.0$ ) for galaxies in the range  $0.5 < z \leq 0.75$  and  $\Delta M_B = -1.32 \pm 0.06$  ( $\chi_\nu^2 = 2.4$ ) for E/S0s in the range  $0.75 < z \leq 1.0$ . Since the  $\chi_\nu^2$  values are so high, the fits are poor. We find poor fits for both red and blue galaxies and both redshift ranges. Furthermore, there is no obvious correlation between the half-light radius and absolute magnitude. We find many more compact luminous E/S0 galaxies (both red and blue) than Schade found. As with the Sersic parameter, we find a significant change in  $\Delta M_B$  for fainter ‘blue’ galaxies and a much greater variance in  $\Delta M_B$  for ‘blue’ galaxies. One effect that is difficult to take into account is the ‘color-selection effect’. The most rapidly evolving ‘blue’ galaxies at  $0.75 < z < 1.0$  will become ‘red’ at  $0.5 < z < 0.75$ . This could increase the evolution seen amongst red galaxies and decrease the evolution seen amongst ‘blue’ galaxies.

While we find a poor fit to the magnitude size relationship, we find a much better fit to the photometric plane. Graham (2002) demonstrated that the ‘photometric plane’ variables  $R_e, \mu_e, \beta$  are correlated with an rms scatter of 0.170, compared to the ‘fundamental plane’ variables  $R_e, \mu_e, \sigma_0$  which are correlated with an rms scatter of 0.137 for a selection of elliptical and S0 galaxies in the Fornax and Virgo clusters. Márquez et al. (2001) demonstrate that the photometric plane naturally emerges for relaxed Sersic profile systems as a scaling relation between potential energy and mass. The photometric plane:

$$\log(R_e) = a(\log(\beta) + 0.26\mu_e) + b \quad (16)$$

is plotted in Fig. 15 and compared to the Graham (2002) result. The two redshift samples are fit by constraining the slope such that  $a = 0.86$ , the same as in Graham (2002) and then the offset  $b$  is found. We use  $\Delta\beta = 0.5$  in our error assessment. This is the scatter found when comparing the  $\beta$  from GALFIT to the  $\beta$  from the growth curve analysis. The values of  $b$  for each of the samples are tabulated in Table 4. There is a significant shift in the offset from the Graham (2002) result ( $b = -4.85$ ) to our results suggesting evolution in the photometric plane. There is also a small but insignificant change in offset between the different colored galaxies, and the fits for the  $(U - V)_0 > 1.7$  galaxies are better for brighter galaxies. The increased variance in the ‘blue’ galaxies at  $M_B < -20.1$  is consistent with earlier results. Since the earlier results showed that there is no significant variation in  $\langle R_e \rangle$  or  $\langle \beta \rangle$  at  $M_B < -20.1$  with redshift, the shift is caused by a change in surface brightness.

At fainter absolute magnitudes, the offset changes slightly. The offset for ‘blue’ galaxies with  $M_B < -20.1$  at  $z < 0.75$  is similar to that of ‘red’ galaxies with  $M_B < -18.8$  at  $z < 0.75$ . Unfortunately the differences are not significant so this does not demonstrate evolution.

Solving the photometric plane equation for  $\mu_e$ , we find the evolution in surface brightness (for  $M_B < -20.1$ ) and compare our results to the change in surface brightness found in ellipticals in the Sloan Digital Sky Survey (Bernardi et al. 2003) from  $z = 0.06$  to  $z = 0.2$  and in Schade et al. (1999), at  $z = 0.35$  and  $z = 0.78$ . These are shown in the top panel of Fig. 15. The variation is linear with redshift,  $\Delta\mu = -1.74z$ . Using the fundamental plane results for E/S0 galaxies in the DGSS, Gebhardt et al. (2003) find an evolution in surface brightness  $\Delta\mu_e = -3.38z + 4.97z^2 - 4.011z^3$ . Our results are consistent with both the DGSS and the SDSS results.

No evolution is apparent in the structural properties of early-type galaxies over the redshift interval  $0.5 < z \leq 1.0$ , as shown by the lack of variation in the biweight and biweight-scale of  $\beta$  and  $R_e$  at  $M_B < -20.1$  with redshift (Table 4). There are also no significant differences between the sizes of ‘red’ and ‘blue’ galaxies. There is however some indication that the Sersic parameter is slightly larger for bright ( $M_B < -20.1$ ) ‘blue’ galaxies with a wider dispersion (as demonstrated by the larger biweight-scale), as well as increased variance found in the size-magnitude and photometric plane measurements for ‘blue’ galaxies. When fainter galaxies ( $-20.1 < M_B < -18.8$ ) are added into the sample at  $z < 0.75$ , a significant decrease is found in the  $\beta$  values of ‘blue’ galaxies and  $R_e$  values for both samples, as well as a small decrease in  $\beta$  for the ‘red’ sample.

The fainter ‘blue’ galaxies have a significant effect on the offset measured in the size-magnitude relation relative to ‘red’ E/S0 galaxies, but they do not significantly effect the offset in the photometric plane.

The weaker correlations amongst bluer galaxies could be due to three different effects: the bluer galaxies have larger photometric variations; the bluer galaxies haven’t reached dynamical equilibrium; the errors in photometric redshifts are greater for the bluer galaxies. While there is a small color dependency on redshift, it only affects the very bluest ( $(U - V)_0 < 1.2$ ) galaxies and these are not particularly abundant at  $M_B < -20.1$ . The dynamical time for elliptical galaxies is very low: even if ‘blue’ E/S0 galaxies are 10 times less massive than ‘red’ E/S0 galaxies as suggested by Im et al. (2001) the dynamical time would only be a few times  $10^8$  yrs, much lower than the formation timescales and estimated ages. The surface brightness in these galaxies is not as tied to the Sersic parameter and half-light radii as it is for the ‘red’ E/S0s.

We recalculated the above results using the geometric mean half-light radius instead of the semi-major axis, and find that this makes no significant difference to our conclusions.

## 6. THE SPACE DENSITY OF E/S0 GALAXIES

We calculate the space density over the BBD (see Fig. 11) using the bivariate (in  $M_B$  and  $\mu_e$ ) Stepwise Maximum Likelihood (SWML) method of Sodr e & Lahav (1993), modified to incorporate photometric redshift errors using the method of Chen et al. (2003). The bivari-

ate SWML takes into account limits in both magnitude and size, and outputs the correctly weighted space density of galaxies as a function of both absolute magnitude and effective surface brightness (Cross et al. 2001). The luminosity function can be calculated by summing this distribution in the surface brightness direction. Our limits are  $B < 24.5$  mag,  $r_e \geq 0.1''$ ,  $\mu_e^{app} = 25.7$  mag arcsec $^{-2}$  for  $0.5 < z < 0.75$  and  $B < 24.0$  mag,  $r_e \geq 0.1''$ ,  $\mu_e^{app} = 25.2$  mag arcsec $^{-2}$  for  $0.75 < z < 1.0$ . SWML is found to give unbiased results even in very inhomogeneous samples (Willmer 1997; Takeuchi, Yoshikawa & Ishii 2000). SWML gives the shape of the luminosity function, but needs to be normalized independently. We normalize by calculating the number of galaxies in each magnitude bin (after distributing each galaxy by the probability density function in redshift) in the volume limited region of the luminosity function and dividing by the known volume. This is divided by the luminosity function calculated by the SWML method to give a normalization factor in each bin and the mean is found.

### 6.1. The Luminosity Function of E/S0 Galaxies

Fig. 16 shows the luminosity functions of both samples, calculated by summing the two-dimensional space density produced above along the surface brightness direction. The bottom panel shows the full morphologically selected luminosity functions for both redshift ranges and the middle and top panels show the  $(U - V) > 1.38$  and the  $(U - V) > 1.7$  luminosity functions respectively. The square points and solid error bars show the luminosity function for the  $0.5 < z < 0.75$  sample and the triangular points and dashed error bars show the  $0.75 < z < 1.0$  sample. The solid and dashed lines show the best fit Schechter function to each redshift range respectively. Since we cannot determine the luminosity function of the  $0.75 < z < 1.0$  fainter than  $M_B = -19.3$  mag, the faint end slope cannot be properly constrained. Therefore we fit the Schechter function using the faint end slope calculated from the  $0.5 < z < 0.75$  sample in each case. The best fit parameters for all the Schechter functions are tabulated in Table 5.

For the  $0.5 < z < 0.75$  sample, we find  $\phi^* = (1.61 \pm 0.18) \times 10^{-3} h_{0.7}^3 \text{ Mpc}^{-3} \text{ mag}^{-1}$ ,  $M^* - 5 \log h_{0.7} = (-21.1 \pm 0.3)$  mag and  $\alpha = -0.53 \pm 0.17$  and we find that the  $0.75 < z < 1.0$  sample has  $\phi^* = (1.90 \pm 0.16) \times 10^{-3} h_{0.7}^3 \text{ Mpc}^{-3} \text{ mag}^{-1}$ ,  $M^* - 5 \log h_{0.7} = (-21.4 \pm 0.2)$  mag and  $\alpha = -0.53$  (fixed). The evolution in the luminosity function can be accounted for by a decrease in luminosity of  $0.36 \pm 0.36$  mag from  $0.75 < z < 1.0$  to  $0.5 < z < 0.75$  and a decrease of  $(15 \pm 12)\%$  in the number density.

In the  $0.5 < z < 0.75$  range, removing the  $(U - V)_0 < 1.38$  galaxies significantly reduces the number of low luminosity galaxies, changing the faint end slope from  $\alpha = -0.53$  to  $\alpha = 0.24$ .  $M^*$  for the  $0.5 < z < 0.75$  sample is  $0.26 \pm 0.5$  mag fainter and has decreased in space density by  $(39 \pm 11)\%$  compared to the  $0.75 < z < 1.0$  sample. The  $M_B - 5 \log h_{0.7} = -20$  point in the  $0.75 < z < 1.0$  sample suggests a steeper faint end slope for this population. However, the present data are not deep enough to properly constrain it. The  $(U - V)_0 > 1.7$  population is similar in character to the  $(U - V)_0 > 1.38$  population, with an evolution of  $0.22 \pm 0.5$  mag in luminosity and a

$(34 \pm 12)\%$  decrease in number density

In Fig. 17 we compare the  $0.5 < z < 0.75$  LFs with each other and with other rest-frame B luminosity functions for early-type galaxies in this redshift range. In each case, we have converted from the given cosmology to  $\Omega_M = 0.3$ ,  $\Lambda = 0.7$ ,  $H_0 = 70 \text{ km s}^{-1} \text{ Mpc}^{-1}$ . In the case of the COMBO-17 data (Wolf et al. 2003) we have converted from Vega to AB magnitudes by subtracting 0.13 mag (Johnson-B band). All the results are summarised in Table 5. The points with errorbars are those for the morphologically selected luminosity function. The solid lines show our ACS LF, with the thick line showing the full color range, the medium line showing the  $(U - V)_0 > 1.38$  sample and the thin line showing the  $(U - V)_0 > 1.7$  sample. The main difference is between the morphologically-selected sample and the color-selected sample, with little difference between the  $(U - V)_0 > 1.38$  sample and the  $(U - V)_0 > 1.7$  sample. This difference occurs at the faint end, where most of the very blue galaxies are. The thin lines with long dashes and short dashes show the COMBO-17 LFs (Wolf et al. 2003) at  $z = 0.5$  and  $z = 0.7$ , respectively, while the thin dotted line shows the CADIS LF (Fried et al. 2001). The medium thick long-dashed line represents the CFRS (Lilly et al. 1995) LF, and the thick long-dashed line shows the DGSS (Im et al. 2002) luminosity function. The COMBO-17 and CADIS LFs are for objects classified as E-Sa from SED templates and should be best matched to the  $(U - V)_0 > 1.7$  sample. The CFRS should be best matched to the  $(U - V)_0 > 1.38$  sample and the DGSS is morphologically selected and so can be compared to the full sample. Fig. 18 shows the equivalent plot for  $0.75 < z \leq 1.0$ .

The present study has somewhat different parameters from the DGSS, with a fainter  $M_B^*$  and higher  $\phi^*$ , but the luminosity functions are similar, see Fig. 17, with the main differences due to the correlations between  $M_B^*$  and  $\alpha$ . At  $M_B = -21.1$  ( $M_B^*$ ), our  $0.5 < z \leq 0.75$  LF has a space density that is 33% larger. There is closer agreement at other magnitudes. Our LF at  $0.75 < z \leq 1.0$  does not have such close agreement. At  $M_B = -21.4$  ( $M_B^*$ ), our LF has a space density that is 89% larger. The DGSS was not able to constrain the faint end slope, so they used a value  $\alpha = -1.0$ , based on the morphologically selected low redshift luminosity functions calculated from the Second Southern Sky Redshift Survey (SSRS2, Marzke et al. 1998) and the Nearby Optical Galaxy Sample (NOG, Marinoni et al. 1999). Our sample goes almost 2 magnitudes deeper than the DGSS and hence we are able to constrain the faint end slope:  $\alpha = -0.53 \pm 0.17$  is shallower than the DGSS LF, but is much steeper than the color-selected luminosity functions. We can achieve this greater depth ( $I \sim 24$  vs  $I \sim 22$ ) due to a combination of improved pixel scale / point spread function and images that are 1 – 1.5 mag deeper, giving higher resolution images with better signal-to-noise than the DGSS.

When we compare the samples selected with  $(U - V)_0 > 1.38$ , we find that the CFRS is not a good match to the ACS LF. While both have similar values of  $M^*$ , and the values of  $\alpha$  are consistent given the shallow depth of the CFRS, the space density is about twice as high in the CFRS as our measurement. In the higher redshift range, the CFRS luminosity function is a closer match for

$M_B < -21$  mag, but again overestimates the number of galaxies for lower luminosities. This suggests some contamination by late-type galaxies such as Sa/Sbc spirals which the morphological selection removes, as well missing the bluer early-type galaxies.

The  $0.5 < z \leq 0.75$  CADIS LF and  $0.4 < z \leq 0.6$  COMBO-17 LF both closely resemble the ACS  $0.5 < z \leq 0.75$ ,  $(U-V)_0 > 1.7$  LF, with offsets of  $\sim 0.25$  magnitudes either way, which is well within the errors. However the  $0.6 < z \leq 0.8$  COMBO-17 LF has a much lower space density, which is also much lower than the ACS  $0.75 < z \leq 1.0$ ,  $(U-V)_0 > 1.7$  LF. In fact all of the SED selected luminosity functions in the  $0.75 < z \leq 1.0$  range find a much lower space density than the ACS  $0.75 < z \leq 1.0$ ,  $(U-V)_0 > 1.7$  LF. The ACS  $0.75 < z \leq 1.0$  LFs have much better agreement with the DGSS and the CFRS surveys.

The  $0.75 < z \leq 1.04$  CADIS LF, the  $0.8 < z \leq 1.0$  COMBO-17 LF and the ACS  $0.75 < z \leq 1.0$ ,  $(U-V)_0 > 1.7$  LF all have a mean redshift  $\langle z \rangle$  of  $\sim 0.9$ , so it is expected that the luminosity functions should be the same. At  $M_B = -21.1$  ( $M^*$  for the ACS LF), the space density measured in the CADIS LF is 0.43 that of the ACS LF and the space density measured in the COMBO-17 is only 0.13 that of the ACS LF. It appears that many more E/S0 galaxies are missing from the high redshift COMBO-17 and CADIS luminosity functions than expected even considering the color selection in  $(U-V)_0$ . However, there is an additional color selection for COMBO-17, which is the  $R$ -band selection. Galaxies were initially selected to have  $R < 24$ , so the selection is in the rest-frame UV at  $z > 0.75$ . Finally we calculate the luminosity function for our blue E/S0 galaxies. Since we have fewer blue,  $(U-V)_0 < 1.7$ , E/S0 galaxies, we combine all the  $B_{z=0} \leq 24$  mag galaxies together to calculate a LF from  $0.5 < z \leq 1.0$ , see Fig. 19. It has a much steeper faint end slope than the red E/S0 with  $M^* - 5 \log h_{0.7} = (-22.1 \pm 0.4)$  and  $\alpha = -1.19 \pm 0.15$ .

These results show that there is a wide variation in the luminosity functions reported and that selection effects have a systematic effect on the results. In particular, for all color-selected samples, we noted a significant underestimate of the faint end slope compared with morphologically selected samples. The space density of  $M^*$  galaxies also varied greatly from survey to survey.

## 6.2. The Surface Brightness Distribution

The luminosity function of galaxies can be calculated as above by summing the space density in the surface brightness direction, as long as there are not any galaxies missing from the sample due to surface brightness dependent selection criteria (see Cross et al. 2001, Cross & Driver 2002). Fig. 11 demonstrates that we are not missing a significant population of low surface brightness ellipticals. However, the compact ( $r_e < 0.1''$ ) E/S0 galaxies that we removed from the sample do affect the faint end of the luminosity function.

The surface brightness distribution for galaxies with  $0.5 < z \leq 0.75$  is shown in Fig. 20, for all the galaxies and galaxies in different luminosity ranges. It is apparent that the surface brightness distribution peaks at  $\mu_e = 20$  mag arcsec $^{-2}$  for bright galaxies and that any effects of missing galaxies are negligible for  $M_B < -20$  mag and

small for  $-20 < M_B < -19$  mag. However they are important for  $M_B > -19$ . We estimate the effects by adding in all galaxies with  $r_e < 0.1$ , regardless of  $\beta$ , since  $\beta$  will be difficult to accurately measure for such compact objects. At  $z < 0.75$  there are three additional objects, with  $M_B = -19.8, -19.3, -18.6$ . The new luminosity function parameters are shown in Table 5. The faint end slope is steeper, with  $\alpha = -0.75$ .  $M_B^*$  is slightly brighter and  $\phi^*$  is slightly reduced, but these effects are due to the dependency of  $M_B^*$  on  $\alpha$ . It must be emphasized that the additional compact objects may not meet the selection criterion  $\beta > 2$  if observed by a telescope with better resolution, so this new luminosity function is an upper limit.

Fig. 21 shows the surface brightness distributions of the  $0.75 < z \leq 1.0$  sample. At bright  $M_B$  the surface brightness distribution peaks at  $\mu_e \sim 19.5$  mag arcsec $^{-2}$ , brighter than the  $0.5 < z \leq 0.75$  sample by 0.5 mag arcsec $^{-2}$ . This is consistent with the change in surface brightness measured in Fig. 15. The surface brightness distributions suggest that there are no missing compact galaxies with  $M_B < -21$ . There are likely to be some missing galaxies in the range  $-21 < M_B < -20$ , but these only make up a small fraction of the total. For  $M_B > -20$ , the missing fraction is likely to be significant. Amongst galaxies that were discarded, there are two additional galaxies ( $M_B = -20.8, -20.2$ ) that have  $r_e < 0.1$  arcsec. This could increase the space density at  $M_B = -20$  by up to 10%. The low surface brightness limit also becomes important at  $M_B > -20$ . However since this is the limit where our measurements of the half-light radius begins to break down, rather than a detection limit (E/S0 have very high central surface brightnesses), it is unlikely that we are missing any LSBGs.

## 7. DISCUSSION

We find that ‘blue’ E/S0 galaxies make up 30 – 50% of  $M_B < -20.1$  E/S0 galaxies at  $0.5 < z < 0.75$  and 20 – 40% of  $M_B < -20.1$  E/S0 galaxies at  $0.75 < z < 1.0$ . Our results are consistent with both the Menanteau et al. (1999) sample which found similar numbers to these depths and the Im et al. (2001) sample which found only  $\sim 15\%$ . Illustrating this agreement with the latter sample requires that we select galaxies to  $I < 22$  using the Im et al. (2001)  $(V-I)$  color criteria (Figure 1 from that paper). For the present sample this works out to a blue fraction of  $23 \pm 11$  per cent, consistent with the above numbers.

From the analysis of the colors and structural properties of E/S0 galaxies at  $0.5 < z < 1.0$ , it is apparent that bright ( $M_B < -20.1$ ), ‘blue’  $(U-V)_0 < 1.7$  E/S0 galaxies are not significantly different from bright ‘red’  $(U-V)_0 > 1.7$  E/S0 galaxies in terms of their structural parameters. When the stellar population has aged, these galaxies will be only slightly less luminous than the current ‘red’ galaxies, and there will be significant overlap, see Fig. 7. They just have higher current star-formation rates, as measured by the  $N_\tau$  from the Bruzual & Charlot (2003) models. However, these same models indicate that  $(U-V)_0 < 1.7$  E/S0 galaxies are less massive than  $(U-V)_0 > 1.7$  galaxies at the same luminosity. Fainter ( $M_B > -20.1$ ) ‘blue’ E/S0 galaxies are smaller with lower Sersic parameters than their ‘red’ counterparts. These galaxies often have extremely blue colors  $(U-V)_0 < 1.2$

and are likely to be less massive. The evolution tracks Fig. 7 suggests that these will fade by  $\sim 3$  mag as their stellar populations age. This is consistent with these galaxies becoming present day dwarf ellipticals.

The best fits to these models give an increasing rate of formation from  $z \sim 8$  all the way down to  $z \sim 2$  with a short star-formation timescale  $\tau \leq 1$  Gyr. There are only a few objects with longer timescales. The caveat in this modeling is that we have used simple, exponentially decaying star-formation models at a fixed metallicity, with no internal dust corrections since we are comparing observations in only 3 or 4 filters. With 3 broadband filters, there are only 2 color constraints that one can apply to the models, so it is impossible to test for anything beyond a simple variation in age and timescale. Observations of massive ellipticals at low redshifts and modeling support a single main burst, with a short timescale  $0.1 < \tau < 0.3$  and a Salpeter IMF (Pipino & Matteucci 2004).

While there is not enough data to find the best fit solution for a range of metallicities and dust models, it is instructive to estimate the effect that different metallicities or dust will have on the result. As a test for these effects, we recalculated the ages and timescales using metallicities  $Z = 0.008$  and  $Z = 0.05$  to contrast with the results obtained with the solar metallicities ( $Z = 0.02$ ). For each of these metallicities we calculated the ages and star-formation timescales with no dust and using the dust model of Charlot & Fall (2000) assuming a V-band optical depth,  $\tau_V = 1$  and the fraction of light contributed by the ‘ambient’ interstellar medium  $\mu = 0.3$ . These values are the default values used in the Bruzual & Charlot (2003) code, and are close to the “standard” values discussed in Charlot & Fall (2000) and Bruzual & Charlot (2003) for objects with  $T > 10^7$  yr. We recalculated models for star-formation timescales of  $\tau = 0, 1, 0.4, 2.0$  only. We found that the addition of this dust model reduces the average age of each galaxy by  $\sim 10\%$ , depending on the metallicity. Since both age and dust tend to redden a galaxy, the same colors can reflect an old, dust free galaxy or a young dusty galaxy. Age increases with decreasing metallicity and vice-versa due to the absorption of blue light by metals in the atmospheres of stars. We find that  $(\frac{\partial \ln t}{\partial \ln Z}) \sim -0.4$ , lower than the Worthey (1994) value  $(\frac{\partial \ln t}{\partial \ln Z}) \sim -1.5$ . The lower value may be due to the different assumptions. Worthey assumed a single-burst model, whereas we have a continuous exponentially decaying star-formation rate. If these galaxies do have a lower metallicity (as one might expect for intrinsically fainter, likely less massive, bluer galaxies: Tremonti et al. 2003), then they may be older than we estimate.

While the structural properties ( $R_e$  and  $\beta$ ) of bright ‘red’ or ‘blue’ E/S0s do not change significantly with redshift, there is a change in the photometric plane offset, the size-magnitude relation and the luminosity functions demonstrating significant luminosity evolution ( $\sim 0.4$  mag) from  $0.75 < z < 1.0$  to  $0.5 < z < 0.75$ . There are some variations in structural properties between ‘red’ and ‘blue’ galaxies with the ‘red’ galaxies having a smaller variance in the Sersic parameter than ‘blue’ galaxies.

The luminosity evolution measured from the size-magnitude relation is 0.6 mag for ‘red’ galaxies and 0.3 mag for ‘blue’ galaxies. However, there is only a 0.1 mag

change in the  $M^*$  point for the luminosity function of ‘red’ galaxies and 0.3 mag overall. While these values are quite different, the size-magnitude relation does not give a good fit, so one should be careful with the interpretation.  $(U - V)_0 = 2.0$  galaxies are expected to fade by  $\sim 0.25$  mag, regardless of the star-formation timescale, over the  $\sim 1.5$  Gyr time span that separates the median redshift in each bin. Over this same time,  $(U - V)_0 = 1.8$  galaxies are expected to fade by  $\sim 0.55$  mag, so  $\sim 0.4$  mag of evolution is expected. To complicate matters, some objects that were previously considered to be ‘blue’ will have aged sufficiently to be classified as ‘red’. The lower variation in the  $M^*$  point may relate to the smaller variation amongst the very reddest galaxies ( $(U - V)_0 = 2.0$ ), which are also generally the brightest. The expected variation of ‘blue’ galaxies is much wider ranging  $0.2 < \Delta M < 1.5$ , and shows a much greater dependence on the star-formation timescale, so any offset is difficult to predict, especially given that ‘blue’ galaxies will eventually evolve to become ‘red’ galaxies and other new ‘blue’ galaxies may form. Since the evolutionary tracks on Fig 7 suggest that the redder galaxies are more massive than the bluer galaxies, the luminosity evolution is particularly difficult to predict, as more massive ‘blue’ galaxies will become ‘red’. Indeed the galaxies with the most rapid evolution in the restframe  $M_B$  magnitude will also redden the most rapidly, so there is a selection effect operating that will reduce the apparent luminosity evolution observed.

There is a decrease in number density for  $(U - V)_0 > 1.38$  E/S0 galaxies of  $(40 \pm 10\%)$  from  $z = 0.89$  to  $z = 0.64$ , which is very small compared to the factor 3 increase seen in the COMBO-17 and CADIS LFs over the same redshift range. This argues against hierarchical merging being an important evolutionary driver between  $z = 1$  and  $z = 0.5$ , although it could be an important feature at higher redshifts or in lower luminosity objects.

Using deep high resolution optical data we are able to measure the morphological E/S0 luminosity function almost 2 magnitudes deeper than the DGSS and constrain the faint end slope of the  $0.5 < z \leq 0.75$  LF. We find a fairly flat faint end slope  $\alpha = -0.75 \pm 0.13$ , slightly shallower than low redshift luminosity functions for morphologically selected E/S0s but much steeper than color-selected samples. Our values for  $M_B^*$  are consistent with the DGSS but our  $\phi^*$  is larger by  $\sim 40\%$ . This could be due to cosmic variance since both samples are small or due to the differences in morphological selection. To address the latter point, we note that the DGSS sample is selected using the the bulge-to-total ratio ( $B/T > 0.4$ ) and the residual parameter ( $R < 0.06$ ). Fig. 9 of Im et al. (2002) demonstrates that varying the selection criteria a little ( $B/T > 0.3$ ,  $R < 0.08$ ) can increase the sample size by 50%. Changing our selection criteria to  $\beta < 2.5$  reduces our sample size by 15%. These changes are expected to have more of an effect at faint absolute magnitudes, where galaxies have flatter (i.e. lower Sersic number) profiles (Graham & Guzmàn 2003). Thus different morphological selection criteria could explain the variation seen.

Using purely photometric information (color, SED) to select the galaxy sample misses the bluer early types, and may lead to contamination from Sa/Sbc spiral galaxies or other red galaxies. As shown in Figs 17 & 18 there is a

large variation in the measurement of the luminosity function. Indeed using the COMBO-17 results, one would be drawn to the conclusion that there were very few faint early-types ( $\alpha = 0.52$ ) and that there is strong number evolution in the luminosity function, suggesting that many spiral or other galaxies must have become ellipticals over time, e.g. via a high merger rate. The COMBO-17 luminosity functions only sample the brightest luminosities at  $z \sim 1$ , while the ACS and CADIS LFs reach 1.5 mag deeper.

The luminosity function of blue E/S0s is steeper ( $\alpha = -1.19 \pm 0.15$ ) with a bright  $M_B^* - 5 \log h_{0.7} = -22.1 \pm 0.4$ , but a much lower space density  $\phi^* = 2.5 \pm 0.5 \times 10^{-4} h_{0.7}^3 \text{ Mpc}^{-3} \text{ mag}^{-1}$ . Low luminosity systems have a greater proportion of young star-forming systems, suggesting that the more massive galaxies formed earlier or underwent more

rapid star-formation, so they now contain only older stars. These results provide a good fit to the models of Pipino & Matteucci (2004).

## 8. ACKNOWLEDGEMENTS

ACS was developed under NASA contract NAS5-32865 and this research has been supported by NASA grant NAG5-7697. The STScI is operated by AURA Inc., under NASA contract NAS5-26555. We are grateful to Ken Anderson, Jon McCann, Sharon Busching, Alex Framarini, Sharon Barkhouser, and Terry Allen for their invaluable contributions to the ACS project at JHU. We thank Jon McCann for his general computing support, including the development of FITSCUT, that we used to produce the color images. We would like to thank the anonymous referee for his/her useful comments.

## REFERENCES

- Abraham R.G. 2003, ApJ, 586, 745.  
 Beers T., Flynn K., Gebhardt K. 1990, AJ, 100, 32  
 Benítez N. 2000, ApJ, 536, 571  
 Benítez N. et al. (ACS Team) 2004, ApJS, 150, 1  
 Bell E.F. et al. (GEMS Team) 2004, ApJL, 600, 11  
 Bernardi M. et al. 2003, AJ, 125, 1849  
 Bertin E., Arnouts S. 1996, A&AS, 117, 393  
 Blakeslee, J.P. et al. (ACS Team) 2003a, ApJ, 589, 693  
 Blakeslee, J.P., Anderson, K.R., Meurer, G.R., Benítez, N., Magee, D. 2003b, ASP Conf. Ser., Astronomical Data Analysis Software and Systems XII, ed. H. Payne, R. Jedrzejewski, R. Hook, 257.  
 Blakeslee, J.P. et al. (ACS Team) 2003c, ApJL, 596, 143  
 Bouwens R., Broadhurst, T., Illingworth G. 2003, ApJ, 593, 640  
 Bouwens R., Broadhurst, T., Illingworth G., Meurer G., Blakeslee J.P., Franx M., Ford H.C., 2004, ApJ, submitted  
 Capaccioli M. 1989, in Corwin H.G., Bottinelli L. eds, The World of Galaxies, Springer-Verlag, Berlin, p.208  
 Charlot S., Fall S.M. 2000, ApJ, 539, 718  
 Chen H-W, Marzke R.O., McCarthy P.J., Martini P., Carlberg R.G., Persson S.E., Bunker A., Bridge C.R. 2003, ApJ, 586, 745  
 Cohen J.G. Hogg D.W., Blandford R., Cowie L.L., Hu E., Songaila A., Shoppell P., Richberg K. 2000, ApJ, 538, 29  
 Coleman G.D., Wu, C.-C., Weedman, D.W. 1980, ApJS, 43, 393  
 Cross N.J.G., Driver S.P. 2002, MNRAS, 329, 579  
 Cross N.J.G. et al. 2001, MNRAS, 324, 879  
 de Jong R., Lacey C. 2000, ApJ, 545, 781  
 Fernández-Soto A., Lanzetta K.M., Yahil A. 1999, ApJ, 513, 34 (FLY99)  
 Ford H. et al. (ACS Team) 2002, BAAS, 200, 2401  
 Fried J.W. et al. 2001, A&A, 367, 788  
 Gebhardt K. et al. 2003, ApJ, 597, 239  
 Graham A.W., 2002, MNRAS, 334, 859  
 Graham A.W., Guzmán, R. 2003, AJ, 125, 2936  
 Griffiths R. 1994, ApJL, 435, 19  
 Heavens A., Panter B., Jimenez R., Dunlop J. 2004, Nature, in press  
 Im M. et al. 2001, AJ, 122, 750  
 Im M. et al. 2002, ApJ, 571, 136  
 Kashikawa N., et al. 2003, ApJ, 125, 53  
 Kinney A.L., Calzetti D., Bohlin R.C., McQuade K. Storchi-Bergmann T., Schmitt H.R. 1996, ApJ, 467, 38  
 Lilly S.J., Tresse L., Hammer F., Crampton D., Le Fevre O. 1995, ApJ, 455, 108  
 Lin H., Yee H.K.C., Carlberg R.G., Morris S.L., Savicki M., Patton D.R., Wirth G. Shepherd C.W. 1999, ApJ, 518, 533  
 Lupton R.H., Blanton M.R., Fekete G., Hogg D.W., O'Mullane W., Szalay A.S., Wherry N. 2004, PASP, 116, 133  
 Márquez I., Lima Neto G.B., Capelato H., Durret F., Lanzoni B., Gerbal D. 2001, A&A, 379, 767  
 Menanteau F., Ellis R.S., Abraham R.G., Barger A.J., Cowie L.L. 1999, MNRAS, 309, 208  
 Menanteau F., Abraham R.G., Ellis R.S. 2001, MNRAS, 322, 1  
 Menanteau F. et al. (ACS Team) 2004, ApJ, submitted  
 Miley G.K. et al. (ACS Team) 2004, Natur, 427, 47  
 Peng C. Y., Ho L. C., Impey C. D., Rix H.-W., 2002, AJ, 124, 266  
 Pipino A., Matteucci F. 2004, MNRAS, 347, 968  
 Poli F. et al. 2003, ApJ, 593, 1  
 Roche N., Ratnatunga K., Griffiths R.E., Im M., Naim A. 1998, MNRAS, 293, 157  
 Schade D., Barrientos L.F., Lopez-Cruz O. 1997, ApJ, 477, L17  
 Schade D. et al. 1999, ApJ, 525, 31  
 Schlegel D. Finkbeiner D., Davis M. 1998, ApJ, 500, 525  
 Sodr e L.Jr., Lahav O. 1993, MNRAS, 260, 285  
 Takeuchi T.T., Yoshikawa K., Ishii T.T., 2000, ApJS, 129, 1  
 Tran H.D., et al. (ACS Team) 2003, ApJ, 585, 750  
 van den Bergh S. 2001, AJ, 122, 621  
 Williams R.E., et al. 1996, AJ, 112, 1335  
 Willmer C.N.A. 1997, AJ, 114, 898  
 Wolf C., Meisenheimer K., Rix H.-W., Borch A., Dye S., Kleinheinrich M. 2003, A&A, 401, 73  
 Worthey G. 1994, ApJS, 95, 107

TABLE 1  
SUMMARY OF DATA FROM DIFFERENT FIELDS.

Field	Filters	Area ( $\square'$ )	$T_{\text{exp,I}}(\text{s})^{\text{a}}$	E(B-V)	A(I) <sup>a</sup>	ZP(I) <sup>a,b</sup>	N(E/S0)
NGC4676	g,V,I	7.8	4070	0.017	0.030	25.947	12
UGC10214	g,V,I	10.7	8180	0.009	0.017	25.947	17
TN1338	g,r,i,z	11.7	11700	0.096	0.193	25.655	14
TN0924	V,i,z	11.7	11800	0.057	0.115	25.655	19
HDFN	i+FLY99	5.8	5600	0.012	0.024	25.655	10

<sup>a</sup>The exposure time, extinction and zeropoint are given for the F775W or F814W filter, since this was used for measurements of the structural parameters.

<sup>b</sup>This is the zeropoint for a 1s exposure.

TABLE 2

SUMMARY OF GALAXY PROPERTIES FOR ALL 72 E/S0s IN THE SAMPLE. THE GALAXIES IN BOLD ARE THOSE IN THE VOLUME LIMITED SAMPLE  $M_B < -20.1$ ,  $R_e > 0.8$  kpc. THE HORIZONTAL LINE SEPARATES THOSE WITH  $0.5 < z \leq 0.75$  FROM THOSE WITH  $0.75 < z \leq 1.0$ . WITHIN EACH REDSHIFT RANGE THEY ARE IN ORDER OF THEIR  $(U - V)_0$  COLOR.

No	RA	Dec	$z^a$	$M_B$	$(U - V)_0$	$\beta$	$R_e / \text{kpc}$
01	16 06 16.9	55 26 53.4	0.65	-19.14	0.61	2.56	0.96
02	16 06 06.5	55 26 50.9	0.66	-18.88	0.75	2.57	1.46
<b>03</b>	<b>09 24 19.1</b>	<b>-22 01 28.1</b>	<b>0.73</b>	<b>-20.44</b>	<b>0.83</b>	<b>2.09</b>	<b>2.88</b>
04	16 06 16.5	55 23 44.2	0.52	-19.26	0.84	2.61	1.63
<b>05</b>	<b>12 46 18.1</b>	<b>30 42 53.5</b>	<b>0.66</b>	<b>-20.75</b>	<b>0.84</b>	<b>7.18</b>	<b>2.09</b>
06	13 38 30.0	-19 44 20.0	0.61	-19.36	0.96	3.50	0.74
07	09 24 27.4	-22 01 37.9	0.72	-18.81	0.97	2.38	1.15
<b>08</b>	<b>09 24 21.4</b>	<b>-22 01 15.9</b>	<b>0.73</b>	<b>-20.30</b>	<b>1.16</b>	<b>5.18</b>	<b>1.92</b>
09	09 24 25.4	-22 02 46.9	0.73	-19.33	1.17	2.32	1.45
10	12 46 14.7	30 45 32.7	0.72	-18.83	1.17	2.39	1.63
<b>11</b>	<b>16 06 14.9</b>	<b>55 26 52.8</b>	<b>0.53</b>	<b>-20.51</b>	<b>1.22</b>	<b>2.19</b>	<b>1.36</b>
<b>12</b>	<b>09 24 23.2</b>	<b>-22 03 04.3</b>	<b>0.71</b>	<b>-20.32</b>	<b>1.27</b>	<b>2.25</b>	<b>2.47</b>
<b>13</b>	<b>12 46 18.3</b>	<b>30 43 25.5</b>	<b>0.63</b>	<b>-21.26</b>	<b>1.29</b>	<b>5.26</b>	<b>4.04</b>
14	09 24 17.4	-22 01 38.5	0.73	-19.55	1.40	4.86	1.61
<b>15</b>	<b>09 24 20.0</b>	<b>-22 03 15.2</b>	<b>0.69</b>	<b>-20.23</b>	<b>1.40</b>	<b>9.01</b>	<b>2.08</b>
<b>16</b>	<b>12 46 12.3</b>	<b>30 45 21.2</b>	<b>0.70</b>	<b>-22.83</b>	<b>1.41</b>	<b>5.03</b>	<b>3.30</b>
<b>17</b>	<b>12 46 08.6</b>	<b>30 41 52.7</b>	<b>0.66</b>	<b>-20.75</b>	<b>1.42</b>	<b>4.29</b>	<b>2.89</b>
<b>18</b>	<b>13 38 31.5</b>	<b>-19 45 05.7</b>	<b>0.66</b>	<b>-20.97</b>	<b>1.71</b>	<b>5.25</b>	<b>1.44</b>
<b>19</b>	<b>09 24 24.5</b>	<b>-22 00 42.3</b>	<b>0.70</b>	<b>-21.37</b>	<b>1.74</b>	<b>4.01</b>	<b>2.49</b>
<b>20</b>	<b>09 24 15.7</b>	<b>-22 01 33.4</b>	<b>0.71</b>	<b>-21.73</b>	<b>1.74</b>	<b>6.47</b>	<b>2.07</b>
<b>21</b>	<b>16 06 02.0</b>	<b>55 24 51.3</b>	<b>0.59</b>	<b>-20.97</b>	<b>1.76</b>	<b>3.22</b>	<b>2.91</b>
<b>22</b>	<b>12 36 57.1</b>	<b>62 12 10.8</b>	<b>0.67<sup>a</sup></b>	<b>-21.18</b>	<b>1.93</b>	<b>4.34</b>	<b>2.72</b>
23	13 38 21.8	-19 44 31.7	0.66	-19.62	1.94	10.00	1.43
24	12 46 17.3	30 42 28.2	0.55	-19.40	1.96	3.40	0.88
<b>25</b>	<b>12 46 15.2</b>	<b>30 43 57.4</b>	<b>0.53</b>	<b>-20.45</b>	<b>1.97</b>	<b>3.00</b>	<b>2.96</b>
<b>26</b>	<b>09 24 19.2</b>	<b>-22 03 00.2</b>	<b>0.64</b>	<b>-21.77</b>	<b>1.98</b>	<b>2.73</b>	<b>6.36</b>
<b>27</b>	<b>12 37 00.2</b>	<b>62 12 35.0</b>	<b>0.56<sup>a</sup></b>	<b>-20.32</b>	<b>1.99</b>	<b>3.16</b>	<b>2.07</b>
28	13 38 22.0	-19 44 38.7	0.68	-20.00	1.99	5.13	1.29
29	12 36 46.2	62 11 51.4	0.50 <sup>a</sup>	-19.43	2.00	3.24	0.88
<b>30</b>	<b>09 24 20.1</b>	<b>-22 03 11.4</b>	<b>0.53</b>	<b>-21.30</b>	<b>2.00</b>	<b>6.59</b>	<b>11.03</b>
<b>31</b>	<b>12 46 17.8</b>	<b>30 43 38.7</b>	<b>0.55</b>	<b>-20.87</b>	<b>2.01</b>	<b>3.14</b>	<b>1.48</b>
<b>32</b>	<b>12 36 49.9</b>	<b>62 12 46.0</b>	<b>0.68<sup>a</sup></b>	<b>-21.08</b>	<b>2.02</b>	<b>5.86</b>	<b>4.40</b>
33	16 06 18.0	55 25 03.2	0.89	-19.80	1.23	2.33	2.06
<b>34</b>	<b>16 06 20.3</b>	<b>55 24 44.2</b>	<b>0.99</b>	<b>-21.68</b>	<b>1.24</b>	<b>3.66</b>	<b>1.56</b>
<b>35</b>	<b>13 38 20.7</b>	<b>-19 43 30.9</b>	<b>0.97</b>	<b>-21.23</b>	<b>1.30</b>	<b>5.35</b>	<b>1.74</b>
<b>36</b>	<b>09 24 21.9</b>	<b>-22 02 54.8</b>	<b>0.76</b>	<b>-21.21</b>	<b>1.39</b>	<b>2.02</b>	<b>1.32</b>
<b>37</b>	<b>09 24 16.3</b>	<b>-22 01 17.1</b>	<b>0.77</b>	<b>-20.52</b>	<b>1.39</b>	<b>9.42</b>	<b>2.42</b>
<b>38</b>	<b>09 24 26.1</b>	<b>-22 03 31.0</b>	<b>0.88</b>	<b>-20.47</b>	<b>1.40</b>	<b>2.16</b>	<b>2.77</b>
<b>39</b>	<b>12 36 45.8</b>	<b>62 12 46.7</b>	<b>0.90<sup>a</sup></b>	<b>-21.52</b>	<b>1.46</b>	<b>6.17</b>	<b>2.79</b>
<b>40</b>	<b>09 24 20.9</b>	<b>-22 03 08.2</b>	<b>0.75</b>	<b>-20.99</b>	<b>1.55</b>	<b>4.49</b>	<b>3.45</b>
41	16 06 03.6	55 24 54.0	0.84	-19.78	1.56	4.79	3.42
<b>42</b>	<b>13 38 22.4</b>	<b>-19 42 52.8</b>	<b>0.90</b>	<b>-20.94</b>	<b>1.58</b>	<b>2.73</b>	<b>4.68</b>
<b>43</b>	<b>13 38 24.4</b>	<b>-19 41 34.0</b>	<b>1.00</b>	<b>-21.17</b>	<b>1.66</b>	<b>8.75</b>	<b>2.55</b>
<b>44</b>	<b>13 38 30.5</b>	<b>-19 42 44.1</b>	<b>0.97</b>	<b>-22.12</b>	<b>1.70</b>	<b>7.13</b>	<b>7.46</b>
<b>45</b>	<b>13 38 31.4</b>	<b>-19 44 36.8</b>	<b>0.94</b>	<b>-21.21</b>	<b>1.72</b>	<b>4.29</b>	<b>1.66</b>
<b>46</b>	<b>16 06 04.6</b>	<b>55 24 44.5</b>	<b>0.84</b>	<b>-21.52</b>	<b>1.74</b>	<b>2.64</b>	<b>2.92</b>
47	13 38 21.5	-19 44 39.8	0.85	-20.07	1.74	9.86	0.92
<b>48</b>	<b>13 38 27.6</b>	<b>-19 42 12.6</b>	<b>0.98</b>	<b>-20.35</b>	<b>1.81</b>	<b>2.04</b>	<b>3.79</b>
<b>49</b>	<b>13 38 30.1</b>	<b>-19 44 14.7</b>	<b>0.93</b>	<b>-20.68</b>	<b>1.86</b>	<b>3.21</b>	<b>1.53</b>
<b>50</b>	<b>09 24 27.3</b>	<b>-22 02 54.3</b>	<b>0.90</b>	<b>-21.39</b>	<b>1.91</b>	<b>6.33</b>	<b>1.81</b>
<b>51</b>	<b>16 06 01.0</b>	<b>55 24 57.6</b>	<b>0.82</b>	<b>-21.52</b>	<b>1.93</b>	<b>5.00</b>	<b>3.33</b>
<b>52</b>	<b>13 38 25.4</b>	<b>-19 43 33.3</b>	<b>0.96</b>	<b>-21.00</b>	<b>1.96</b>	<b>3.05</b>	<b>1.42</b>
<b>53</b>	<b>09 24 16.4</b>	<b>-22 01 11.6</b>	<b>0.85</b>	<b>-21.52</b>	<b>1.97</b>	<b>5.21</b>	<b>3.96</b>



TABLE 2—*Continued*

No	RA	Dec	$z^a$	$M_B$	$(U - V)_0$	$\beta$	$R_e$ / kpc
<b>54</b>	<b>16 05 59.4</b>	<b>55 26 16.0</b>	<b>0.81</b>	<b>-22.47</b>	<b>1.97</b>	<b>8.38</b>	<b>5.18</b>
55	16 06 13.5	55 24 45.8	0.84	-19.68	1.99	2.43	1.50
<b>56</b>	<b>16 06 08.6</b>	<b>55 26 04.0</b>	<b>0.79</b>	<b>-20.52</b>	<b>1.99</b>	<b>2.52</b>	<b>1.52</b>
<b>57</b>	<b>16 06 14.9</b>	<b>55 27 12.7</b>	<b>0.84</b>	<b>-20.78</b>	<b>1.99</b>	<b>4.29</b>	<b>1.06</b>
<b>58</b>	<b>09 24 28.0</b>	<b>-22 01 38.2</b>	<b>0.98</b>	<b>-20.11</b>	<b>1.99</b>	<b>4.82</b>	<b>1.43</b>
<b>59</b>	<b>12 46 17.1</b>	<b>30 44 09.0</b>	<b>0.86</b>	<b>-20.25</b>	<b>2.01</b>	<b>2.73</b>	<b>3.03</b>
<b>60</b>	<b>12 46 20.5</b>	<b>30 42 54.8</b>	<b>0.88</b>	<b>-21.00</b>	<b>2.01</b>	<b>2.81</b>	<b>4.15</b>
<b>61</b>	<b>12 36 54.8</b>	<b>62 13 03.9</b>	<b>0.95<sup>a</sup></b>	<b>-20.26</b>	<b>2.01</b>	<b>2.98</b>	<b>0.89</b>
62	16 06 00.7	55 24 59.5	0.76	-19.93	2.02	2.90	2.42
63	12 46 07.7	30 44 41.7	0.86	-20.03	2.02	3.28	1.21
<b>64</b>	<b>16 06 11.3</b>	<b>55 27 45.3</b>	<b>0.86</b>	<b>-22.38</b>	<b>2.02</b>	<b>5.56</b>	<b>3.72</b>
<b>65</b>	<b>12 36 42.8</b>	<b>62 12 42.3</b>	<b>0.85<sup>a</sup></b>	<b>-21.64</b>	<b>2.03</b>	<b>4.49</b>	<b>2.35</b>
<b>66</b>	<b>09 24 26.7</b>	<b>-22 01 01.7</b>	<b>0.97</b>	<b>-20.40</b>	<b>2.04</b>	<b>4.19</b>	<b>2.03</b>
<b>67</b>	<b>12 46 16.6</b>	<b>30 44 48.2</b>	<b>0.79</b>	<b>-20.13</b>	<b>2.04</b>	<b>4.93</b>	<b>1.64</b>
<b>68</b>	<b>12 36 55.1</b>	<b>62 13 11.5</b>	<b>0.97<sup>a</sup></b>	<b>-21.90</b>	<b>2.05</b>	<b>3.90</b>	<b>3.82</b>
<b>69</b>	<b>12 36 56.3</b>	<b>62 12 20.4</b>	<b>0.93<sup>a</sup></b>	<b>-21.39</b>	<b>2.06</b>	<b>5.38</b>	<b>3.48</b>
<b>70</b>	<b>13 38 31.0</b>	<b>-19 44 41.9</b>	<b>0.79</b>	<b>-21.47</b>	<b>2.06</b>	<b>6.36</b>	<b>3.67</b>
<b>71</b>	<b>12 36 43.5</b>	<b>62 11 43.0</b>	<b>0.77<sup>a</sup></b>	<b>-22.09</b>	<b>2.07</b>	<b>5.15</b>	<b>3.55</b>
<b>72</b>	<b>16 05 59.5</b>	<b>55 26 13.3</b>	<b>0.88</b>	<b>-20.43</b>	<b>2.08</b>	<b>3.28</b>	<b>1.27</b>

<sup>a</sup>The redshifts are  $z_{\text{best}}$  in all cases apart from those marked which are spectroscopic redshifts in the HDFN ( $RA \sim 189.2$ ,  $DEC \sim 62.2$ ).

TABLE 3

SUMMARY OF CLOSEST BAND TO REST-FRAME U AND REST-FRAME V. THESE BANDS ARE USED TO GIVE THE BEST ESTIMATE OF THE RESTFRAME  $(U - V)_0$ , WHICH IS USED TO COMPARE TO THE COLOR OR SED SELECTED SAMPLES OF CFRS, CADIS AND COMBO-17.

Field	Band1 ( $z < 0.75$ )	Band2 ( $z < 0.75$ )	Band1 ( $z \geq 0.75$ )	Band2 ( $z \geq 0.75$ )
UGC10214	F475W	F814W	F606W	F814W
NGC4676	F475W	F814W	F606W	F814W
TN1338	F475W	F850LP	F625W	F850LP
TN0924	F606W	F850LP	F606W	F850LP
HDFN	F450W	F814W	F606W	J <sub>KPNO</sub>

TABLE 4  
COMPARISON OF STRUCTURAL PROPERTIES OF EARLY-TYPE GALAXIES.

Sample	$\langle \beta \rangle^a$	$\langle R_e \rangle^b$	$R_e$ vs $M_B^c$	$\chi_\nu^2$	$R_e$ vs $(\log(\beta) + 0.26\mu_e)^d$	$\chi_\nu^2$
$M < -20.1, R_e > 0.8$						
$z < 0.75$ all	$4.4 \pm 0.4$	$2.5 \pm 0.2$	$-0.78 \pm 0.07$	3.0	$-4.56 \pm 0.03$	1.2
$z < 0.75$ red	$4.2 \pm 0.5$	$2.5 \pm 0.4$	$-0.74 \pm 0.08$	4.1	$-4.54 \pm 0.04$	0.6
$z < 0.75$ blue	$4.7 \pm 0.8$	$2.5 \pm 0.3$	$-0.96 \pm 0.17$	1.8	$-4.60 \pm 0.06$	1.9
$z > 0.75$ all	$4.4 \pm 0.3$	$2.6 \pm 0.2$	$-1.32 \pm 0.06$	2.4	$-4.49 \pm 0.03$	0.9
$z > 0.75$ red	$4.3 \pm 0.3$	$2.7 \pm 0.3$	$-1.34 \pm 0.06$	2.3	$-4.47 \pm 0.03$	0.6
$z > 0.75$ blue	$4.7 \pm 1.0$	$2.5 \pm 0.3$	$-1.29 \pm 0.12$	3.0	$-4.55 \pm 0.05$	1.7
$M < -18.8, R_e > 0.73$						
$z < 0.75$ all	$3.7 \pm 0.3$	$2.0 \pm 0.2$	$-0.72 \pm 0.06$	2.3	$-4.63 \pm 0.03$	1.4
$z < 0.75$ red	$4.1 \pm 0.4$	$2.0 \pm 0.3$	$-0.76 \pm 0.08$	2.8	$-4.61 \pm 0.04$	1.6
$z < 0.75$ blue	$2.7 \pm 0.4$	$1.8 \pm 0.2$	$-0.60 \pm 0.12$	1.8	$-4.67 \pm 0.04$	1.1

<sup>a</sup> $\beta$  is the Sersic parameter, see Eqn 2. The average in this case is the biweight and the error is the biweight-scale.

<sup>b</sup> $R_e$  is the intrinsic half-light radius in kpc. The average in this case is the biweight and the error is the biweight-scale.

<sup>c</sup>The offset in the size-magnitude relation compared to  $z = 0$ .

<sup>d</sup>The offset in the photometric plane at  $z = 0$  is  $-4.85$ .

TABLE 5

SUMMARY OF  $B$ -BAND LUMINOSITY FUNCTION SCHECHTER PARAMETERS FOR EARLY TYPE GALAXIES. ALL VALUES HAVE BEEN CORRECTED TO  $\Omega_m = 0.3$ ,  $\Lambda = 0.7$  AND  $H_0 = 70 \text{ km s}^{-1} \text{Mpc}^{-1}$ .

Sample	Selection	Redshift	$M_B^* - 5 \log h_{0.7}$	$\phi^* / 10^{-4} h_{0.7}^3$	$\alpha$
ACS	Morph	$0.5 < z < 0.75$	$-21.1 \pm 0.3$	$16.1 \pm 1.8$	$-0.53 \pm 0.17$
ACS	Morph	$0.75 < z < 1.0$	$-21.4 \pm 0.2$	$18.9 \pm 1.6$	$-0.53$
DGSS	Morph	$0.6 < z < 1.2$	$-21.75 \pm 0.15$	$7.7 \pm 2.2$	$-1.0$
ACS	$(U - V) > 1.38$	$0.5 < z < 0.75$	$-20.6 \pm 0.5$	$12.9 \pm 1.5$	$+0.24 \pm 0.49$
ACS	$(U - V) > 1.38$	$0.75 < z < 1.0$	$-20.8 \pm 0.2$	$21.2 \pm 1.8$	$+0.24$
CFRS	$(U - V) > 1.38$	$0.5 < z < 0.75$	$-20.74$	$31.5$	$-0.37$
CFRS	$(U - V) > 1.38$	$0.75 < z < 1.0$	$-22.84$	$1.9$	$-2.01$
ACS	$(U - V) > 1.7$	$0.5 < z < 0.75$	$-20.6 \pm 0.5$	$10.3 \pm 1.4$	$+0.35 \pm 0.59$
ACS	$(U - V) > 1.7$	$0.75 < z < 1.0$	$-20.7 \pm 0.2$	$15.5 \pm 1.5$	$+0.35$
COMBO-17	SED (E+Sa)	$0.4 < z < 0.6$	$-20.69 \pm 0.16^a$	$9.8 \pm 4.1$	$+0.52$
COMBO-17	SED (E+Sa)	$0.6 < z < 0.8$	$-21.10 \pm 0.16^a$	$4.6 \pm 1.2$	$+0.52$
COMBO-17	SED (E+Sa)	$0.8 < z < 1.0$	$-20.96 \pm 0.21^a$	$1.6 \pm 1.4$	$+0.52$
CADIS	SED (E+Sa)	$0.5 < z < 0.75$	$-20.65 \pm 0.27$	$10.8 \pm 1.1$	$-0.05 \pm 0.22$
CADIS	SED (E+Sa)	$0.75 < z < 1.04$	$-20.48 \pm 0.32$	$4.9 \pm 1.0$	$+0.63 \pm 0.58$
ACS	$(U - V) < 1.7$	$0.5 < z < 1.0$	$-22.1 \pm 0.4$	$2.5 \pm 0.5$	$-1.19 \pm 0.15$
ACS	SB Corr	$0.5 < z < 0.75$	$-21.3 \pm 0.3$	$13.9 \pm 1.8$	$-0.75 \pm 0.13$
ACS	SB Corr	$0.75 < z < 1.0$	$-21.6 \pm 0.2$	$16.7 \pm 0.5$	$-0.75$

<sup>a</sup>The COMBO-17 magnitudes have been corrected by  $-0.13$  to convert  $M_B(\text{Vega})$  to  $M_B(\text{AB})$ .

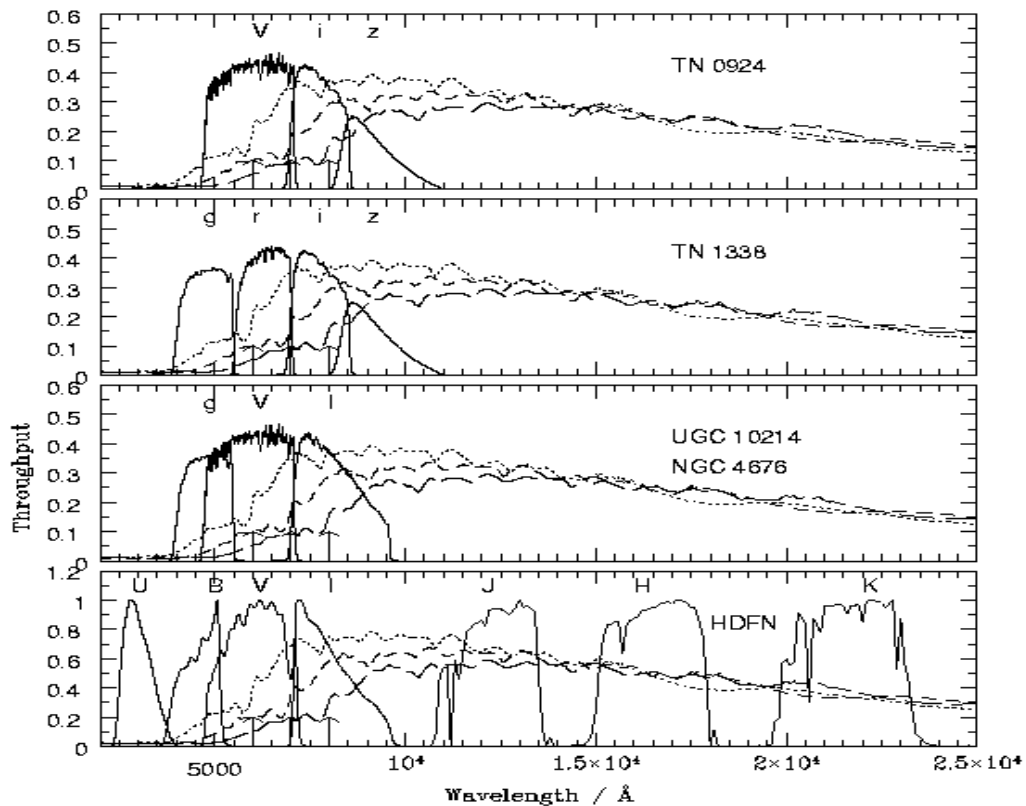


FIG. 1.— The filter sets used in these observations. The top panel shows the three filters used in TN0924,  $Viz$ , the upper-middle panel shows the  $griz$  filters used in TN1338, the lower-middle panel shows the  $gVI$  filters used in UGC10214 and NGC4676 and the bottom panel shows the HDFN, with 7-bands from  $U$  to  $K$ . The dotted, short-dashed and long-dashed curves show the ‘E1’ SED (Benítez et al. 2004, in preparation) at  $z = 0.5, 0.75, 1.0$  respectively. The arrows mark the position of the 4000 Å break at these three redshifts. The 4000 Å break is well within our filter coverage at all redshifts.

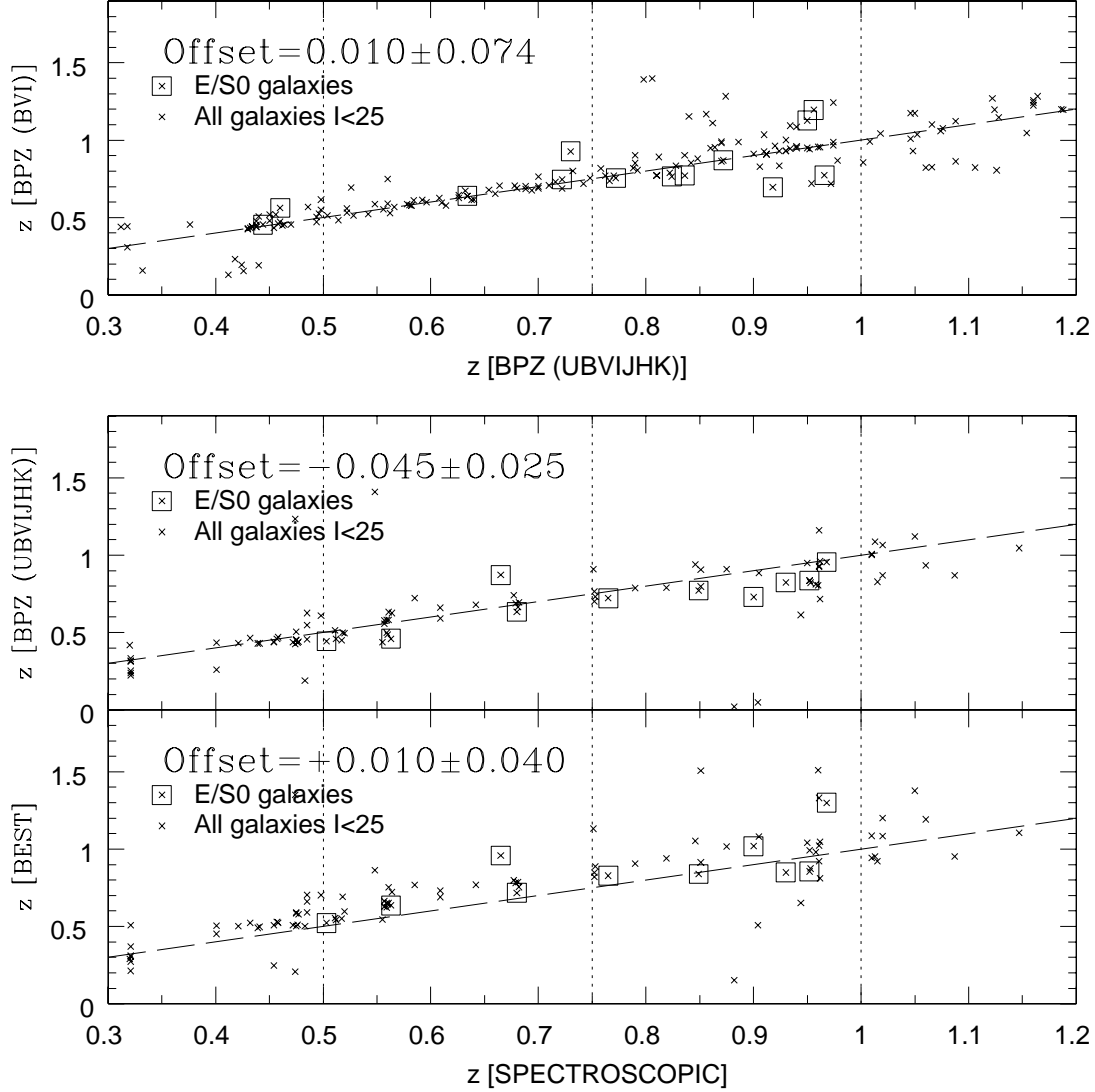


FIG. 2.— The errors in BPZ derived from the HDFN. In the top panel we show the 3-color BPZ redshifts plotted against the 7-color BPZ redshifts for all  $I_{AB} < 25$  galaxies with  $0.3 < z < 1.2$ . The squares surround the galaxies which are morphological elliptical galaxies and have  $0.5 < z_{\text{spec}} < 1.0$  or  $0.5 < z_{\text{BPZ}} < 1.0$  in the 7-color BPZ catalog. There are no outliers in our sample and the systematic offset and error in the redshift each galaxy are small:  $\Delta z/(1+z) = 0.010$  and  $\sigma(\Delta z/(1+z)) = 0.074$  respectively. We then compare 7-color BPZ photometric redshifts to the smaller sample of objects with spectroscopic redshifts in the middle panel. We find that there is a significant offset between the 7-color BPZ and the spectroscopic redshifts. We correct for this offset, see Eqn 1 and calculate  $z_{\text{best}}$ , which is plotted in the lower panel.

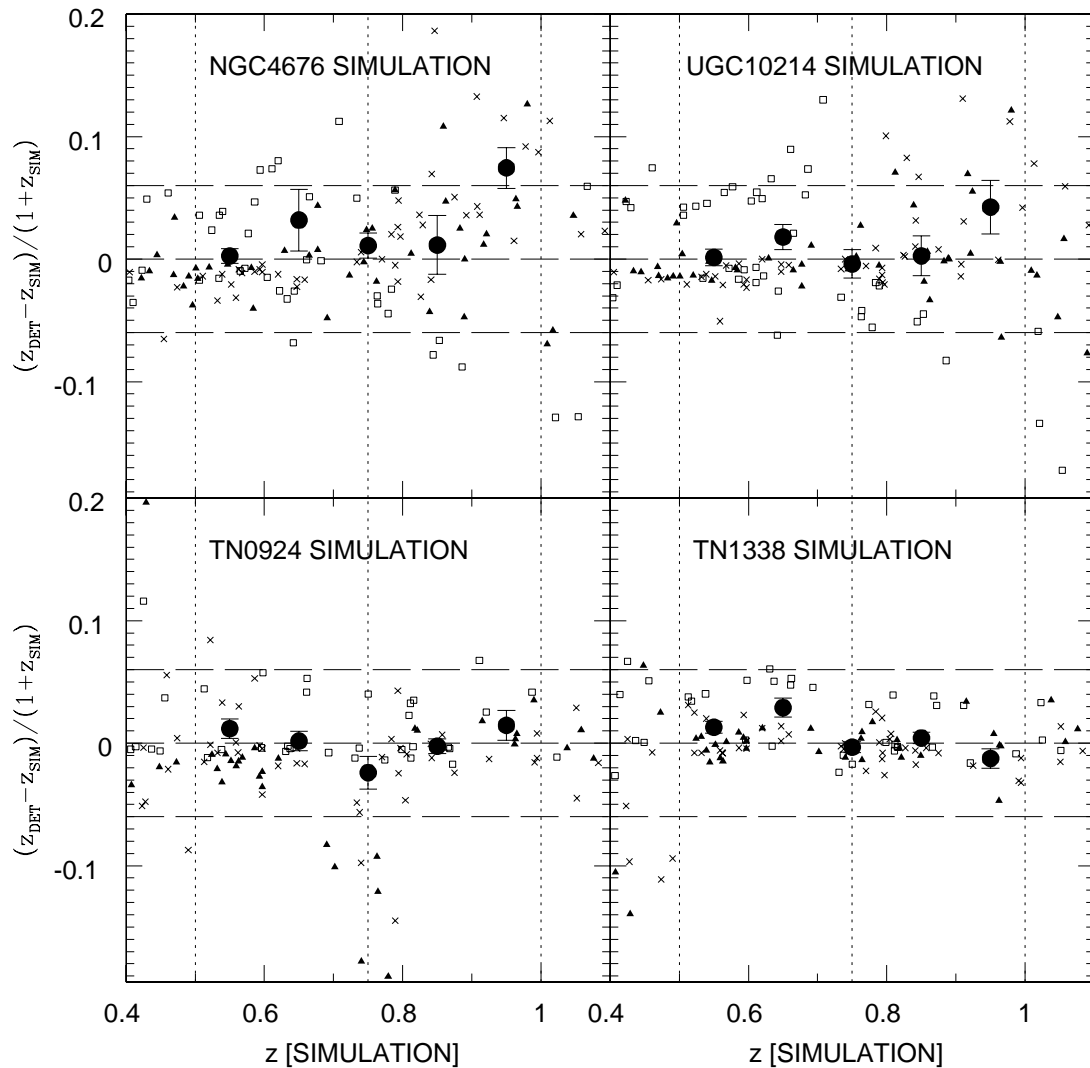


FIG. 3.— The 4 panels show the results of the 4 simulations, TN0924, TN1338, NGC4676 and UGC10214 as labeled. The y axis is the difference in the redshift,  $(z_{\text{detection}} - z_{\text{simulation}}) / (1 + z_{\text{simulation}})$ . The open squares represent objects with an ‘El’ SED, the crosses represent objects with a ‘Sbc’ SED and the filled triangles represent objects with a ‘Scd’ SED. The circles with errorbars represent the  $3 - \sigma$  clipped mean for the ‘El’ and ‘Sbc’ SEDs. The dotted lines mark out the samples at  $z = 0.5, 0.75, 1.0$ . The dashed lines show the expected mean and standard deviations based on the measurements against spectroscopic data (Benítez et al. 2004, in preparation). There are no significant systematic errors, but galaxies in UGC 10214 and NGC 4676 have large random errors for  $z > 0.85$ .

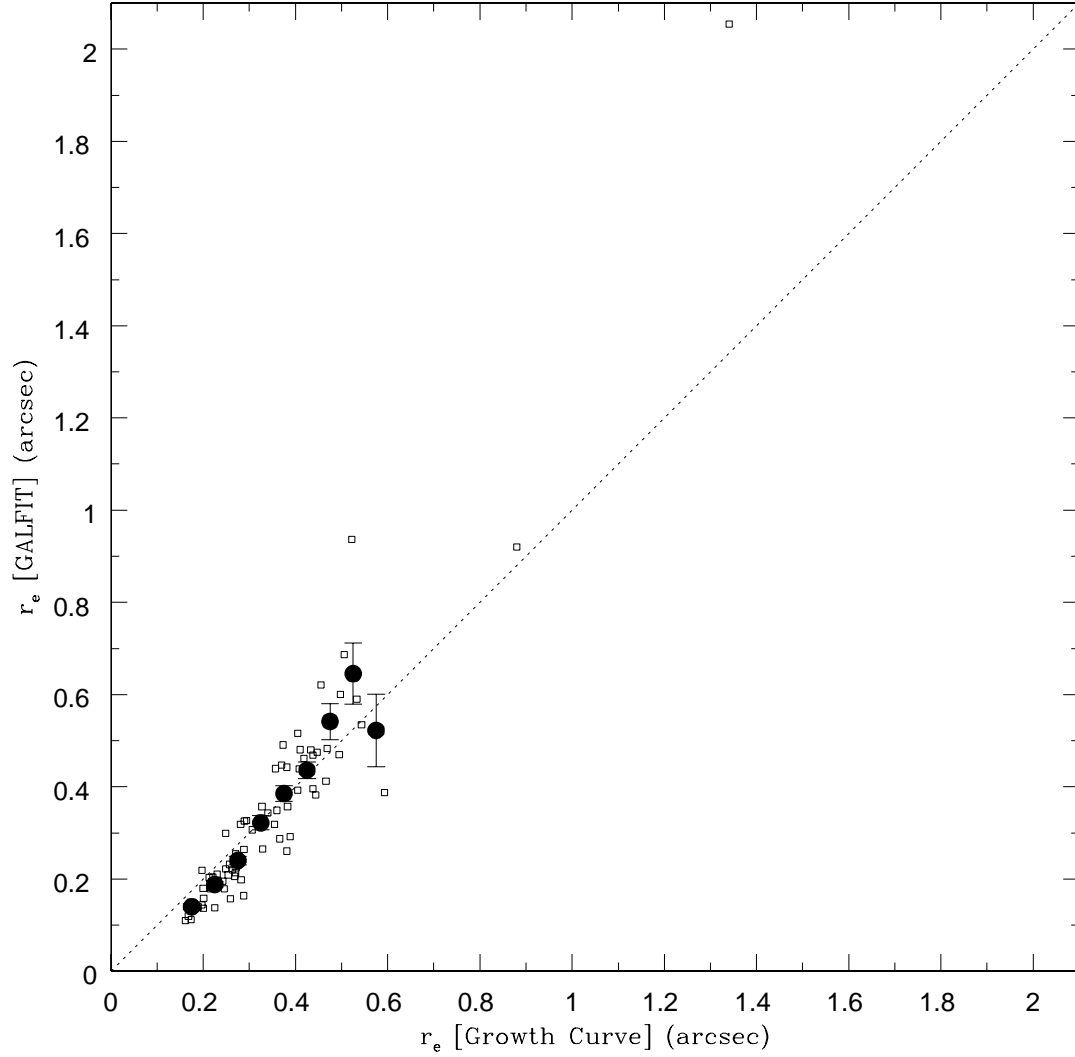


FIG. 4.— This shows a comparison of the half-light radius obtained via a growth curve analysis and the 2-D fitting program GALFIT (Peng et al. 2002) for the ellipticals that we have selected. The PSF correction becomes important for  $r_e < 0.4''$ . The typical error is  $\Delta r_e \sim 0.05''$  for each galaxy, comparable to the pixel size. The much larger errors at  $r_e = 0.55''$  are largely the result of nearby neighbors that affect the photometry. All large outliers were checked manually to see if GALFIT or the growth curve was the source of error. All necessary changes were made.

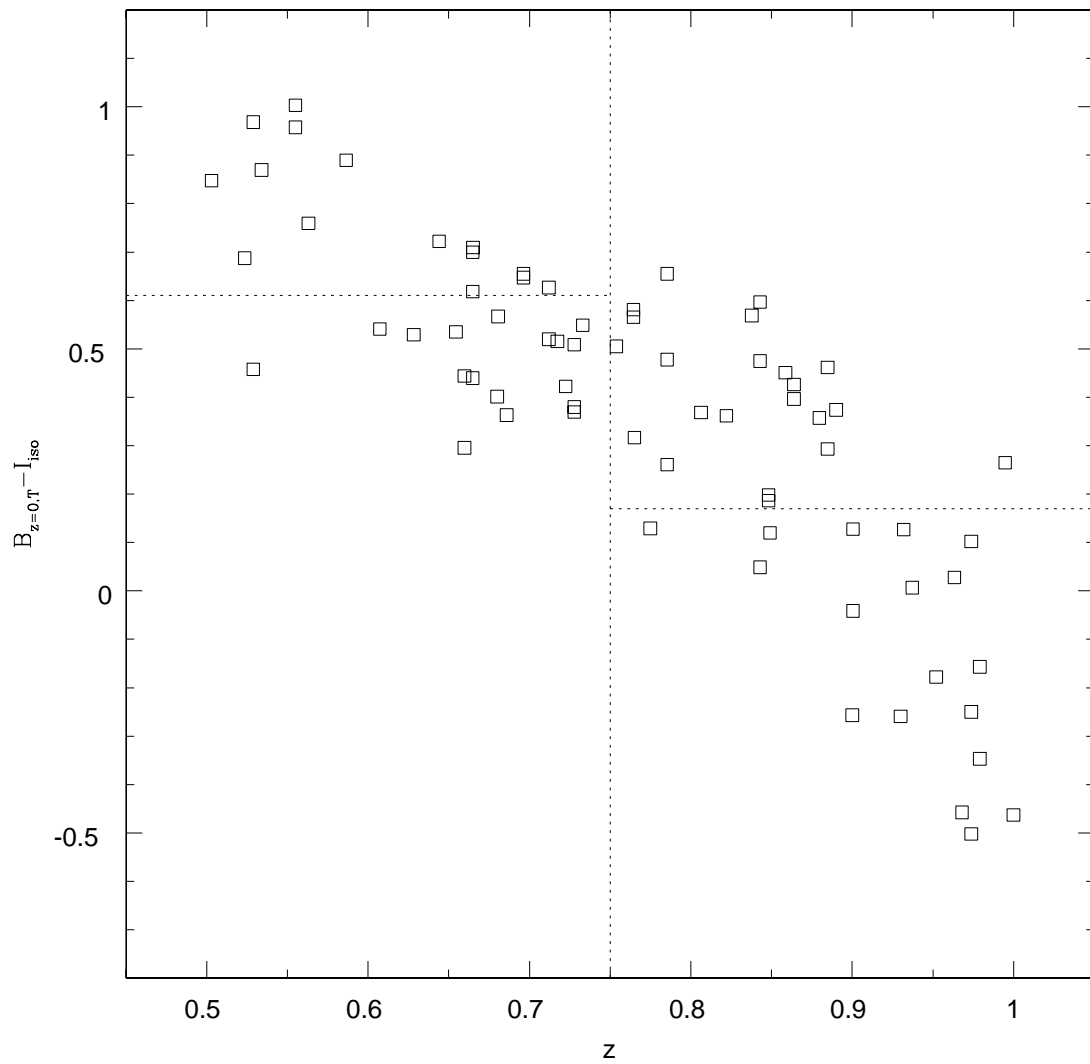


FIG. 5.— This plot shows the generalized k-correction from the measured  $I_{F814W}$  or  $i_{F775W}$  band magnitude to the total rest-frame  $B$  magnitude for early type galaxies in our sample. Objects in the interval  $0.5 \leq z < 0.75$  have an approximate k-correction ( $B_{z=0,T} - I_{iso}$ ) of 0.6 while for objects in the range  $0.75 \leq z < 1.0$ , the k-correction is closer to 0.2.

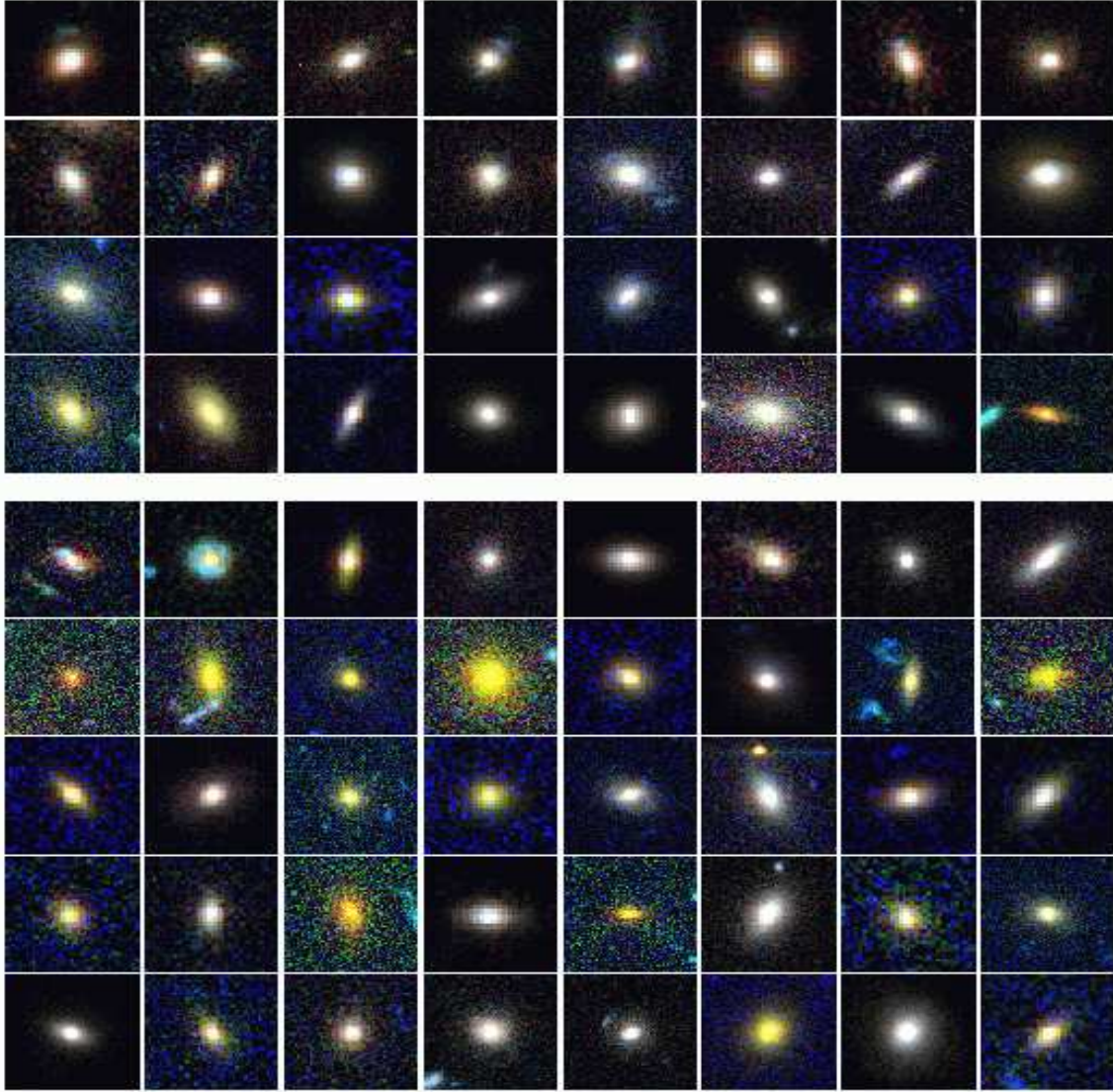


FIG. 6.— This image displays 3-color postage stamps for all of our galaxies. These use an asinh stretch (Lupton et al. 2004) that preserves the colors of bright regions of the galaxy while also showing the fainter regions of these same objects. They are divided into the two redshift samples that we use throughout the analysis and then ordered by  $(U - V)_0$  color, going from bluest (top left) to reddest (bottom right). This is the same order as Table 2. In the case of the HDFN, we display a combination of the ACS i and z only.



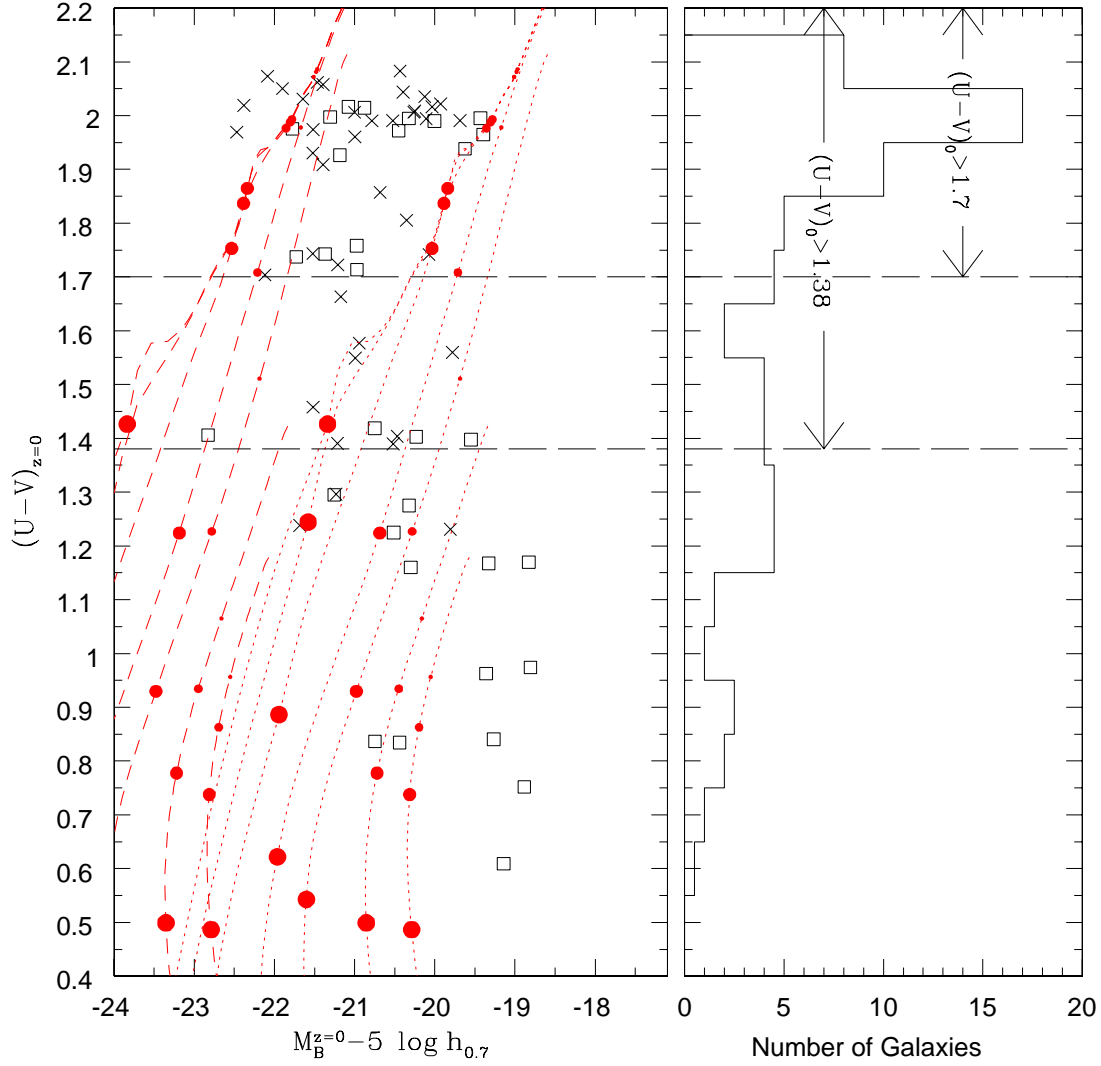


FIG. 7.— The left-hand panel shows the distribution of rest-frame  $(U - V)_0$  color against  $M_B^{z=0}$  for early-type galaxies with  $0.5 < z \leq 0.75$  (squares) and  $0.75 < z \leq 1.0$  (crosses). The dotted lines represent the Bruzual & Charlot (2003) evolutionary tracks for a  $10^{11} M_\odot$  galaxy with solar metallicity and an exponentially decaying star-formation rate with decay timescales  $\tau = 0.1, 0.2, 0.4, 1.0, 2.0, 5.0, 9.0$  Gyr, from left to right. The filled circles represent the age of the galaxy in these models going from 1 Gyr (largest circle) to 7 Gyr (smallest circle) in steps of 2 Gyr. The short dashed lines represent the same tracks for a  $10^{12} M_\odot$  galaxy. The tracks allow us to compare the masses of blue galaxies and red galaxies. The long dashed lines represent the selection criteria used to mimic different color selections employed in the literature. One subsample has  $(U - V)_{z=0} > 1.38$ , to match the CFRS selection and the other has  $(U - V)_{z=0} > 1.7$  to mimic the selections by the COMBO-17 and CADIS (Fried et al. 2001) surveys. The right-hand panel shows the histogram in color for the combined sample. Note the significant number of E/S0s that are bluer than any of the color selections shown.

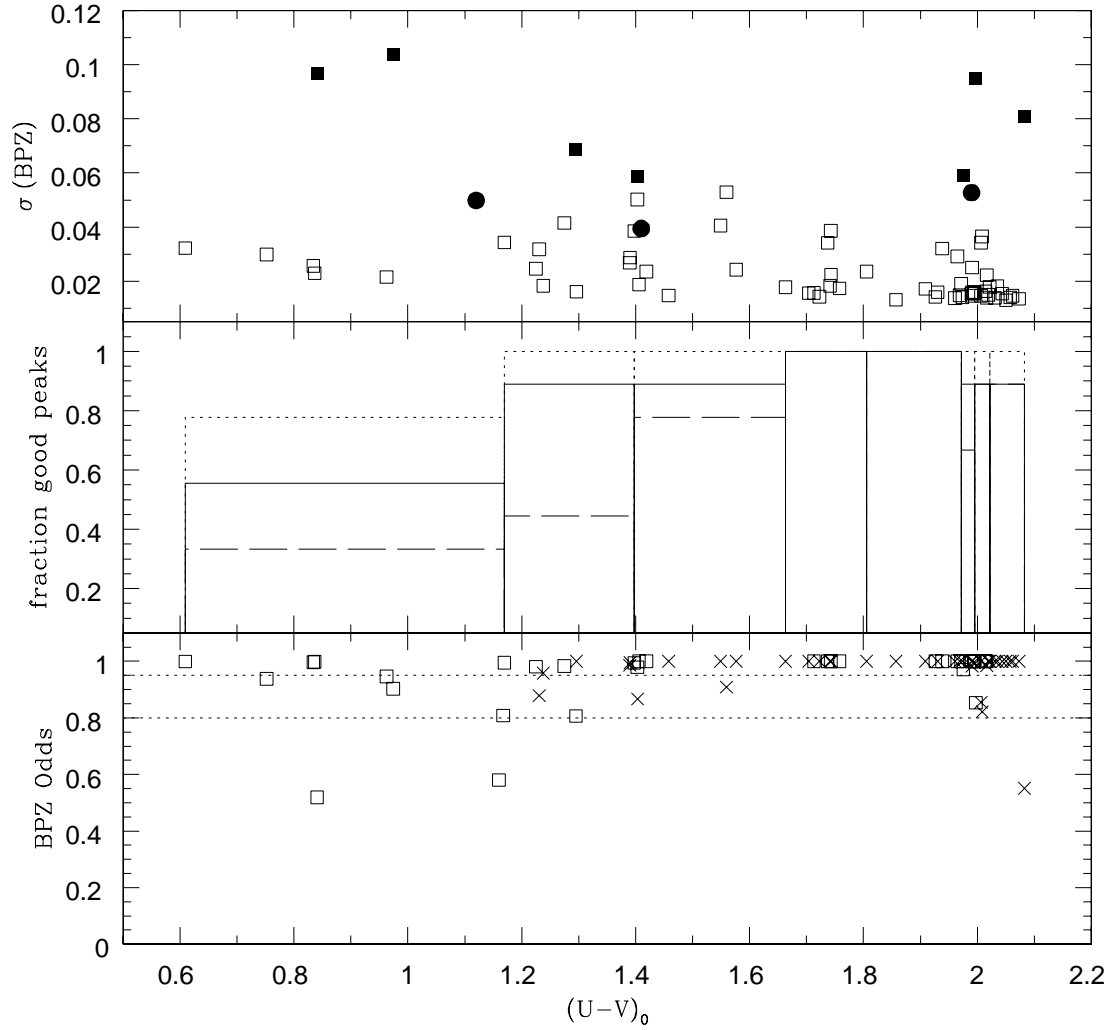


FIG. 8.— This plot shows how the redshift reliability depends on color. The lower panel shows the odds calculated from BPZ against the rest-frame  $(U - V)_0$  color (see §4, Eqn 9 for a definition of the odds). The squares represent  $z < 0.75$  galaxies and the crosses represent  $z > 0.75$  galaxies. This shows that 80% of our objects have good odds, and that the reliability of the redshift does not vary significantly with color or redshift. The middle panel splits the distribution into 8 bins of equal number and plots the number of objects with a single peak in the probability density function (dashed histogram); the solid histogram represents those with one narrow dominant peak (i.e one peak makes up  $> 90\%$  of the integrated probability) and the dotted histogram includes those with multiple overlapping peaks that are in effect a wider peak with  $> 90\%$  of the integrated probability. While the bluer galaxies have more of the wider peaks objects with a single dominant peak make up almost 90% of objects for  $(U - V)_0 > 1.2$ . In the top panel we show the widths of the peaks in the pdf. The open squares show the single narrow peaks, the filled squares show the multiple dominant peaks and the filled circles show the mean from the simulations for an elliptical  $(U - V)_0 = 1.99$ , an Sbc  $(U - V)_0 = 1.40$  and an Scd  $(U - V)_0 = 1.12$ .

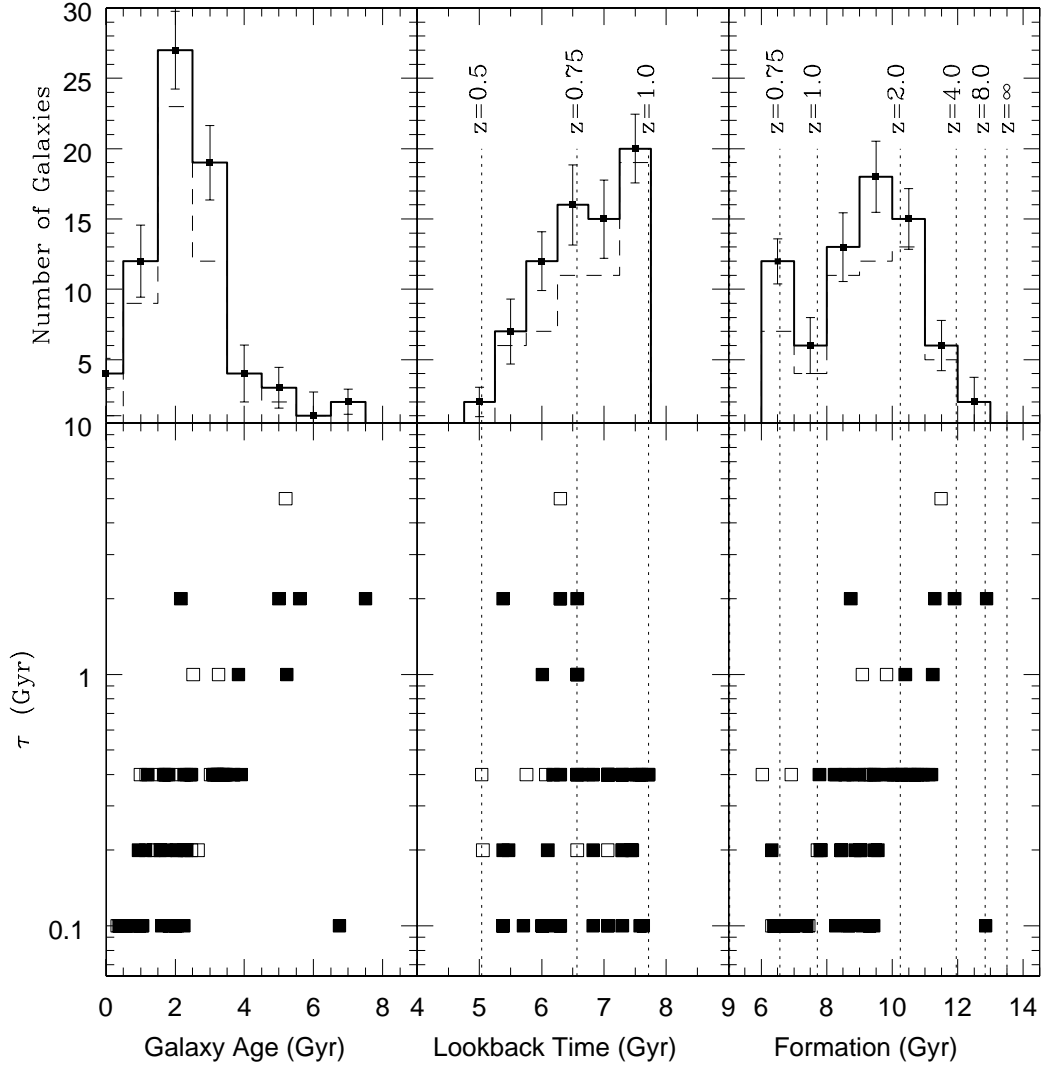


FIG. 9.— The age, lookback time and formation time of early-type galaxies assuming a star formation model with exponential decay timescales  $\tau = 0.1, 0.2, 0.4, 1.0, 2.0, 5.0, 9.0$  Gyr. The bottom left hand panel shows the best fit  $\tau$  versus the best fit age. The bottom middle panel shows the best fit  $\tau$  versus the lookback time, and the bottom right panel shows  $\tau$  versus the formation time, which is the sum of the lookback time and the age. The filled squares represent a volume limited sample. The top panels show the histograms of the age (top left), the lookback time (top middle) and the formation time (top right). The solid histograms show all the objects and the dashed histograms show a volume limited sample. The dotted lines in the lookback time and formation time plots show the equivalent redshift.

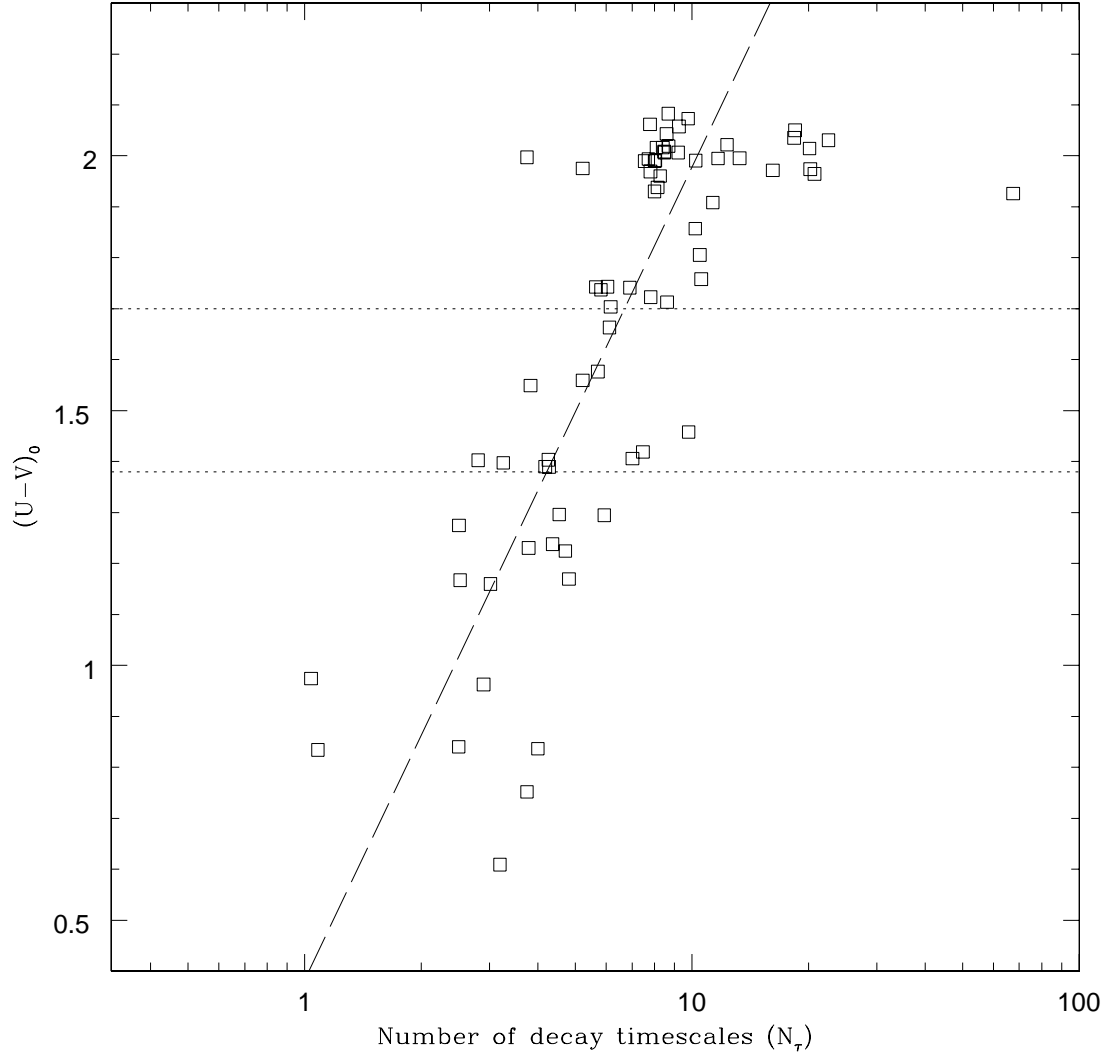


FIG. 10.— This plot compares the rest-frame  $(U - V)_0$  color to the number of decay timescales ( $N_\tau = T/\tau$ ) derived from the Bruzual & Charlot (2003) models. For  $1 < N_\tau < 10$ , there is a strong correlation with  $(U - V)_0 = 1.59 \log(N_\tau) + 0.38$ . For  $N_\tau > 10$ ,  $(U - V)_0 \sim 2.0$ , the rest-frame color of the ‘El’ template from Benítez et al. 2004. The long-dashed line indicates the best fit linear correlation (from a simple least squares calculation). The dotted lines indicate the color cuts for CFRS ( $(U - V)_0 = 1.38$ ) and COMBO-17 and CADIS ( $(U - V)_0 = 1.7$ ).

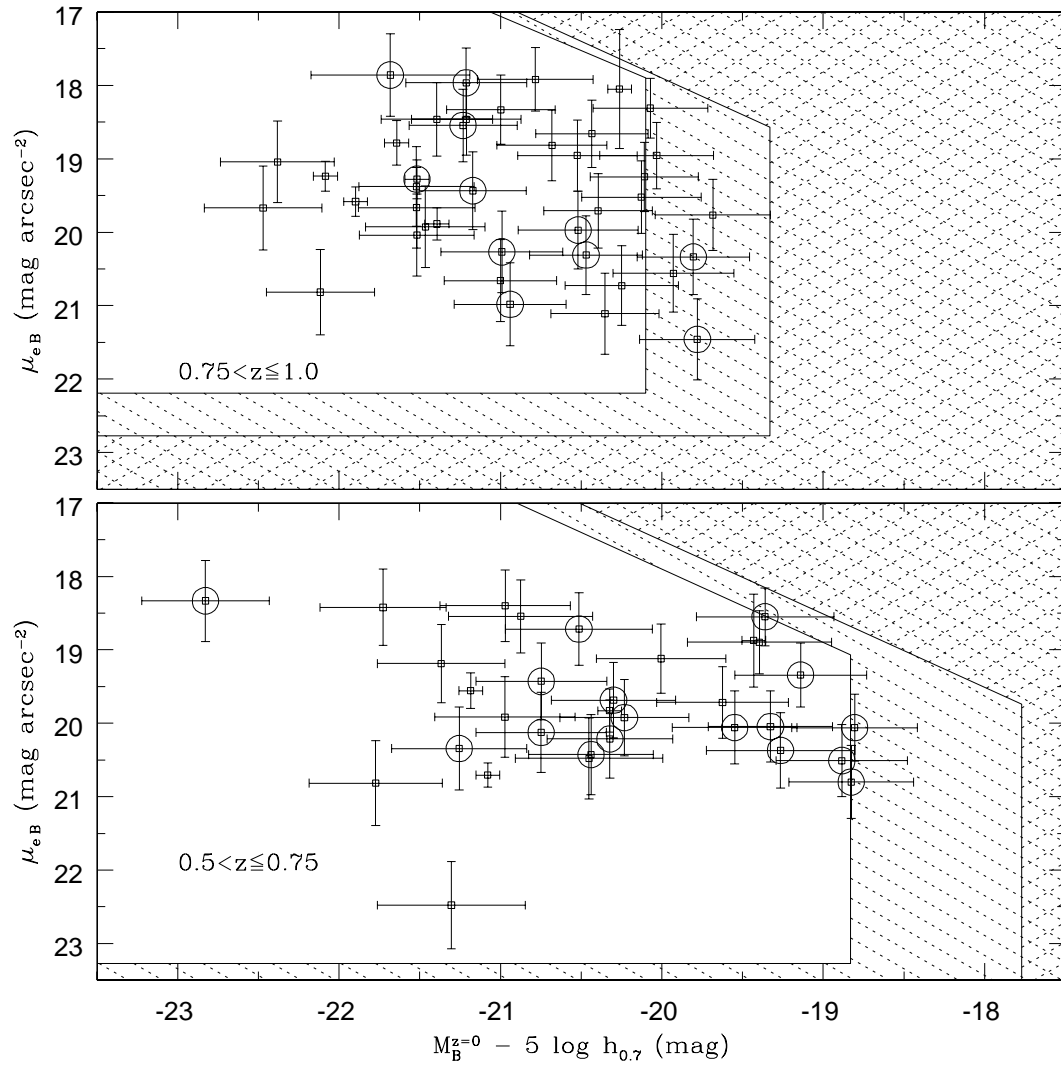


FIG. 11.— The distribution of galaxies in the absolute magnitude and surface brightness plane. The size and magnitude limits are shown at both the low and high redshift end of each sample. All objects in the unshaded area are seen over the same volume. All objects in the cross-hatched area are outside the limits of the survey. The singly shaded region denotes parameter space where galaxies cannot be seen to the maximum redshift. The lower plot shows the  $0.5 < z \leq 0.75$  sample and the upper plot shows the  $0.75 < z \leq 1.0$  sample. The blue E/S0s are circled. They are not separated from the red E/S0s in  $M_B, \mu_e$  space.

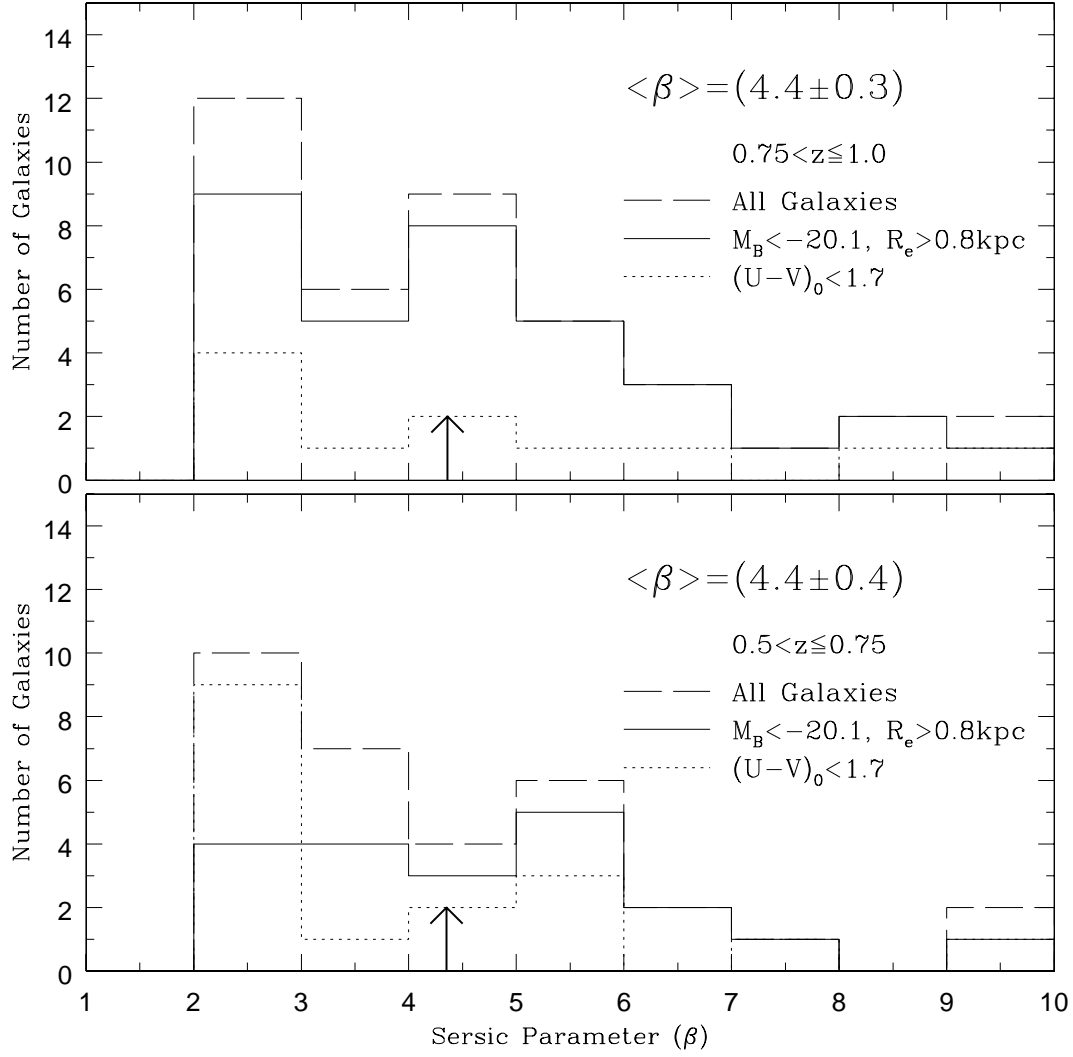


FIG. 12.— We plot the distribution in the Sersic parameter  $\beta$  for each sample (dashed histogram). The solid histogram in each panel is the distribution for equivalent volume limited samples. The distribution of  $\beta$  does not change significantly with redshift. The dotted histogram is the distribution of the ‘blue’ E/S0s. The thick arrow in each panel marks the mean  $\beta$ .

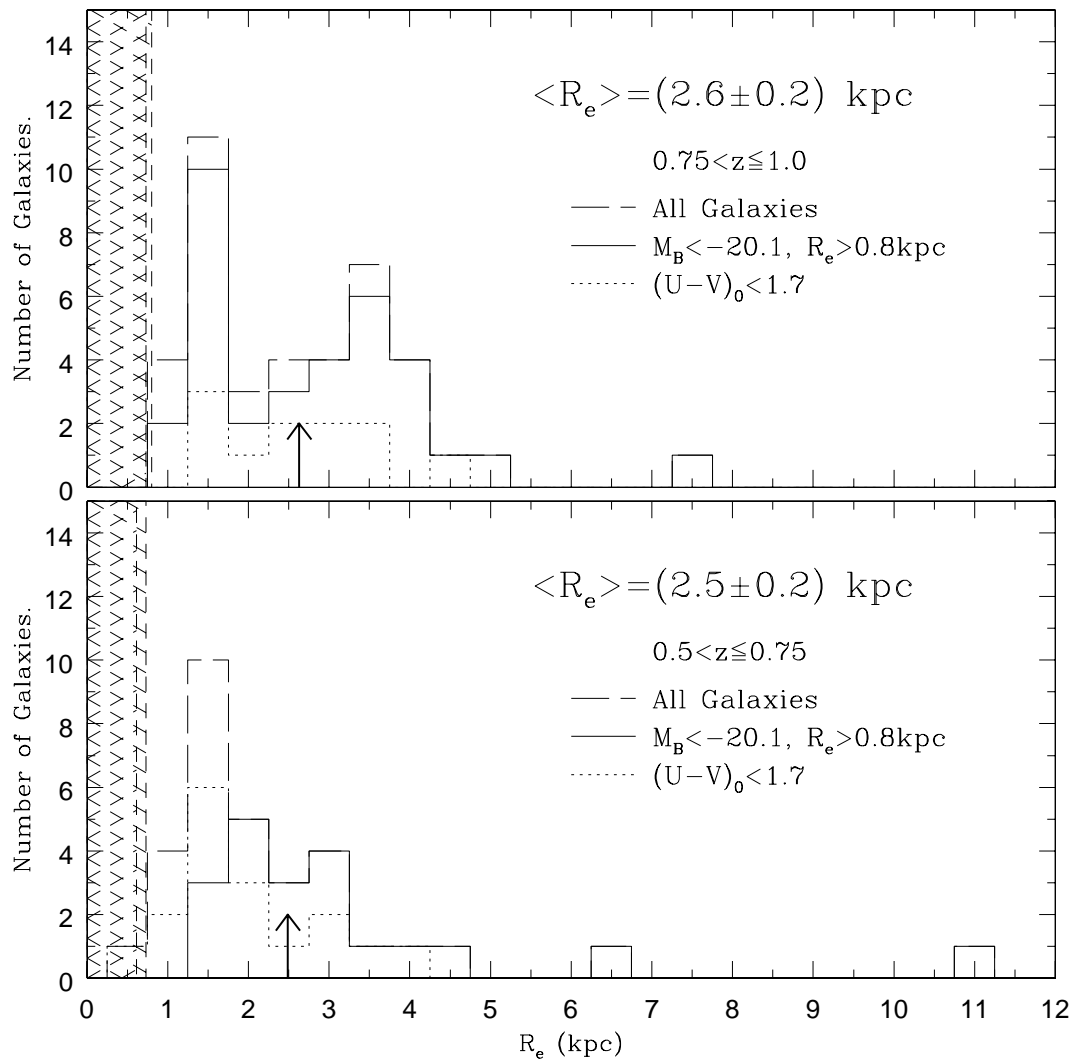


FIG. 13.— The Sersic parameter  $\beta$  distribution for each sample (dashed histogram). The solid histogram is the distribution of the volume limited samples and the dotted histogram is the distribution of the ‘blue’ E/S0s. The thick arrow shows the mean value of  $R_e$ . The shading represents the selection limits in half light radius: the single shading begins at the high-redshift limit of the sample and the cross-hatching begins at the low-redshift limit.

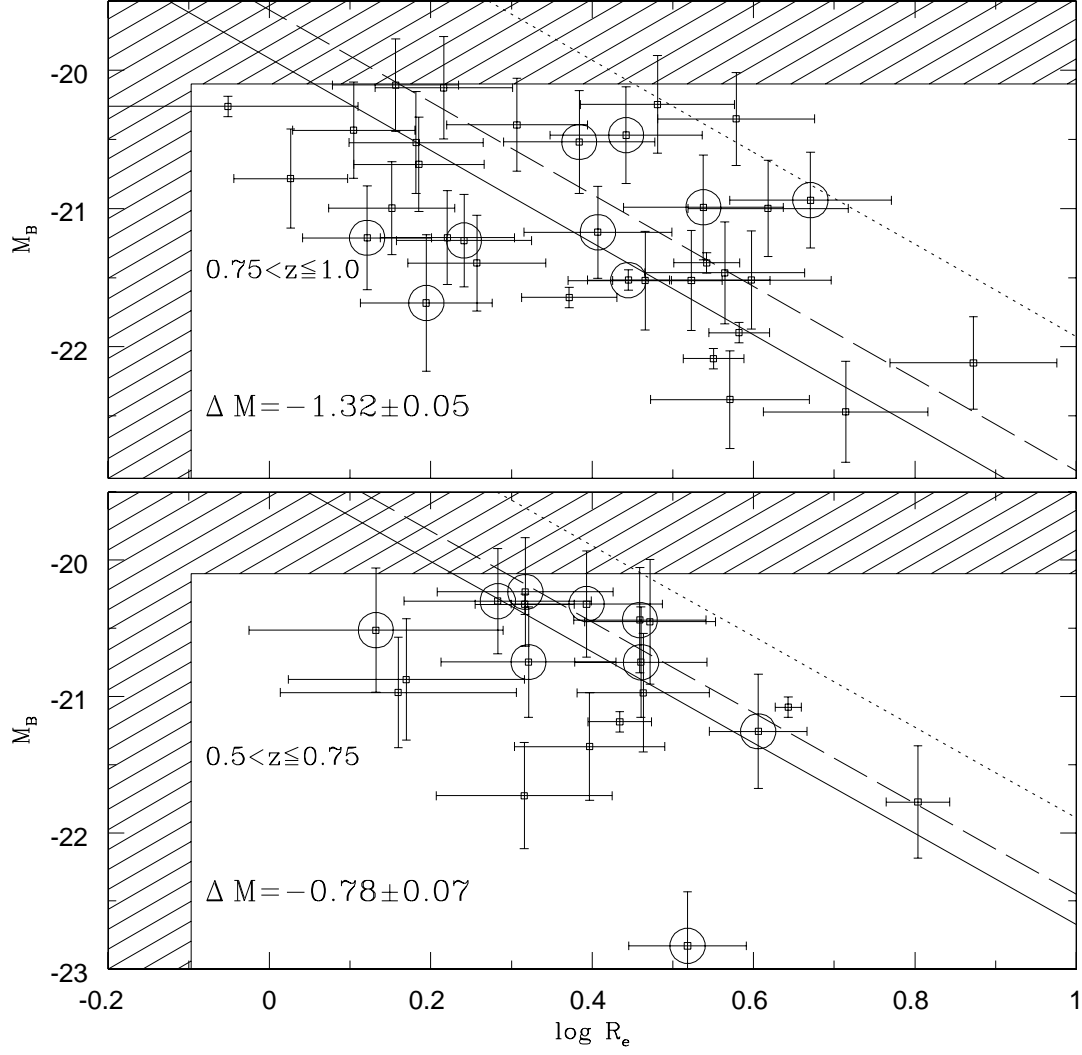


FIG. 14.— This plot shows the distribution of absolute magnitude ( $M_B$ ) versus the logarithm of half-light radius for both E/S0 subsamples considered in this study. The light shading represents the parts of the parameter space where galaxies cannot be seen out to the maximum redshift, and the heavy shading represents the parameter space where galaxies cannot be seen at all. The dotted line is the  $z = 0$  relationship from Schade et al. (1997) corrected to our cosmology. The dashed line is the expected fit from Schade et al. (1999) for each sample and the solid line is our best fit in the volume limited region. The circles mark the positions of blue early-type galaxies. Neither type of galaxy shows strong evidence for a size-magnitude relationship.



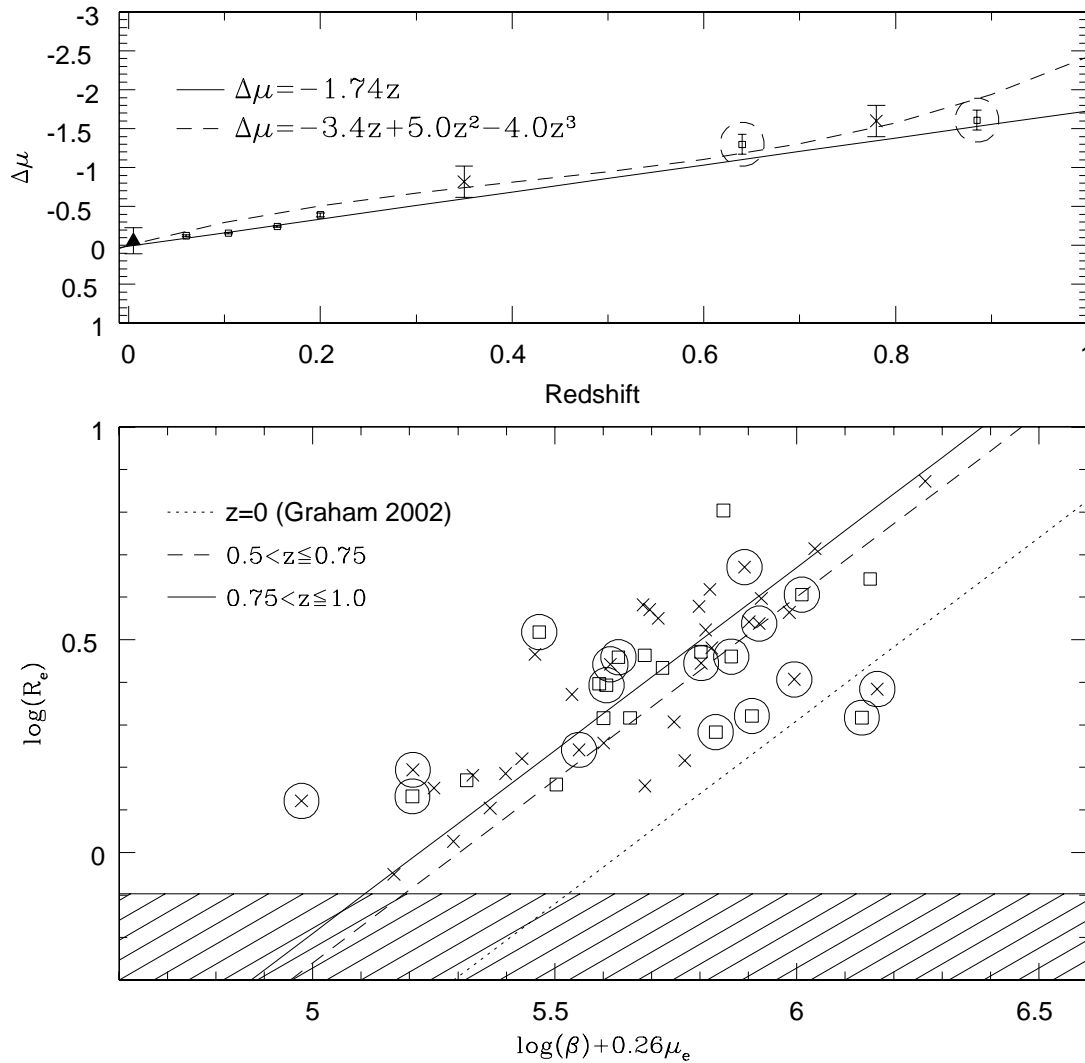


FIG. 15.— The lower panel of this plot shows the photometric plane for elliptical galaxies in our fields. The squares denote the  $0.5 < z \leq 0.75$  sample and the crosses represent the  $0.75 < z \leq 1.0$  sample. Our best fit lines are the solid one for  $0.75 < z \leq 1.0$  and the long-dashed for  $0.5 < z \leq 0.75$ . The  $z = 0$  fit from Graham (2002) is shown by the short dashed line. The blue galaxies are marked by circles. We find good fits to the photometric plane although there are a few outliers amongst the blue E/S0 galaxies. In the top panel, we show the variation in surface-brightness with redshift, calculated from this plot. Our points are marked by the squares ringed by large circles. The Schade et al. (1999) results are marked by crosses, the Bernardi et al. (2003) results are marked by squares and the Graham (2002) result is marked with the triangle. The solid line shows our best fit to these results, and the dashed line is the Gebhardt et al. (2003) best fit.

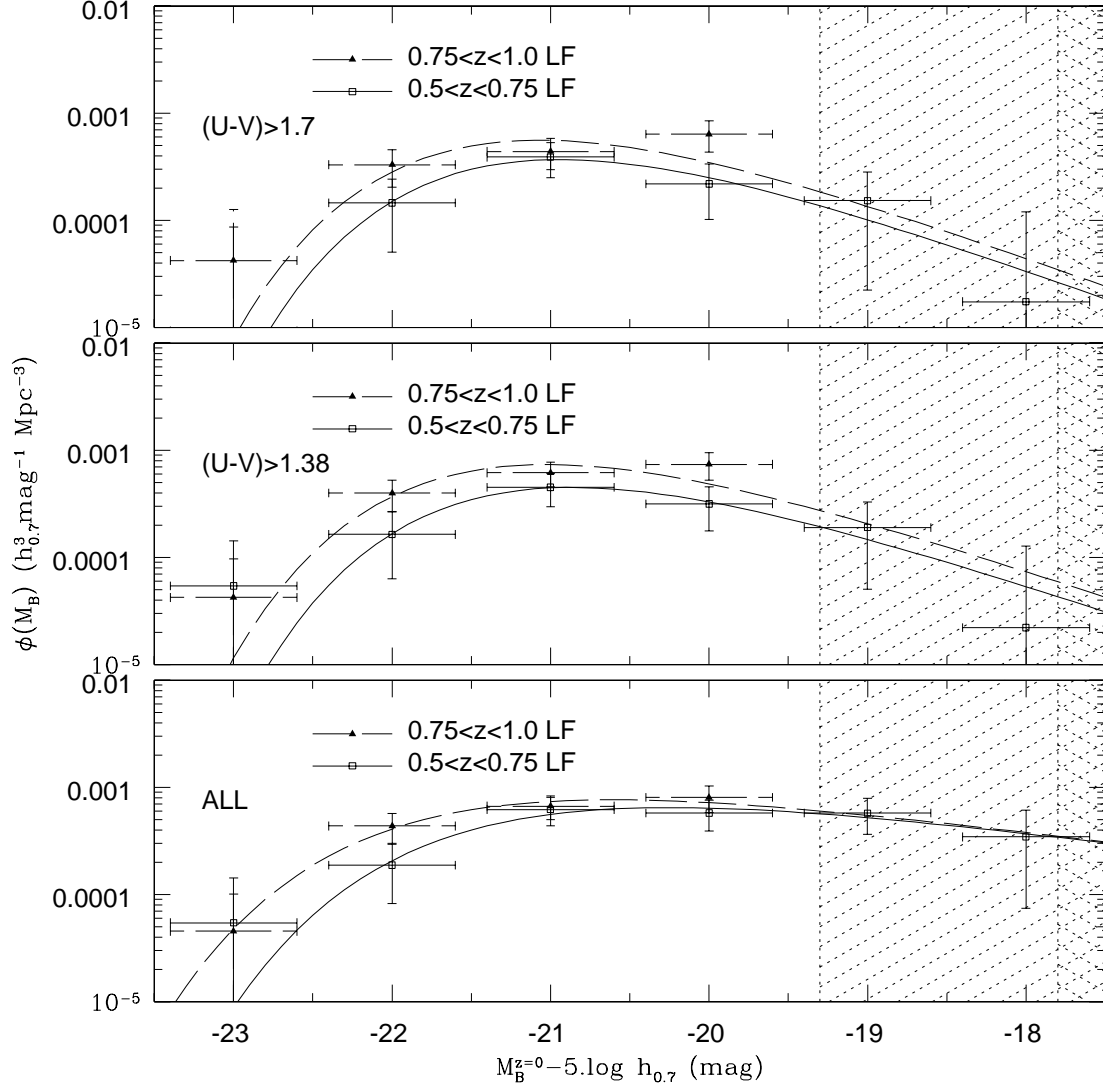


FIG. 16.— The luminosity functions of the  $0.5 < z < 0.75$  (squares with solid error bars) and the  $0.75 < z < 1.0$  (triangles dashed error bars) samples. The bright ends are normalized to the volume limited samples and the lines show the Schechter function fits to each set of points. The single shaded hatching denotes the magnitude limit of the  $0.75 < z < 1.0$  sample and the criss-cross hatching denotes the magnitude limit of the  $0.5 < z < 0.75$  sample. The lower panel shows the morphologically selected samples, the middle panel shows the two  $(U - V)_0 > 1.38$  color selected samples and the upper panel shows the two  $(U - V)_0 > 1.7$  color selected samples.

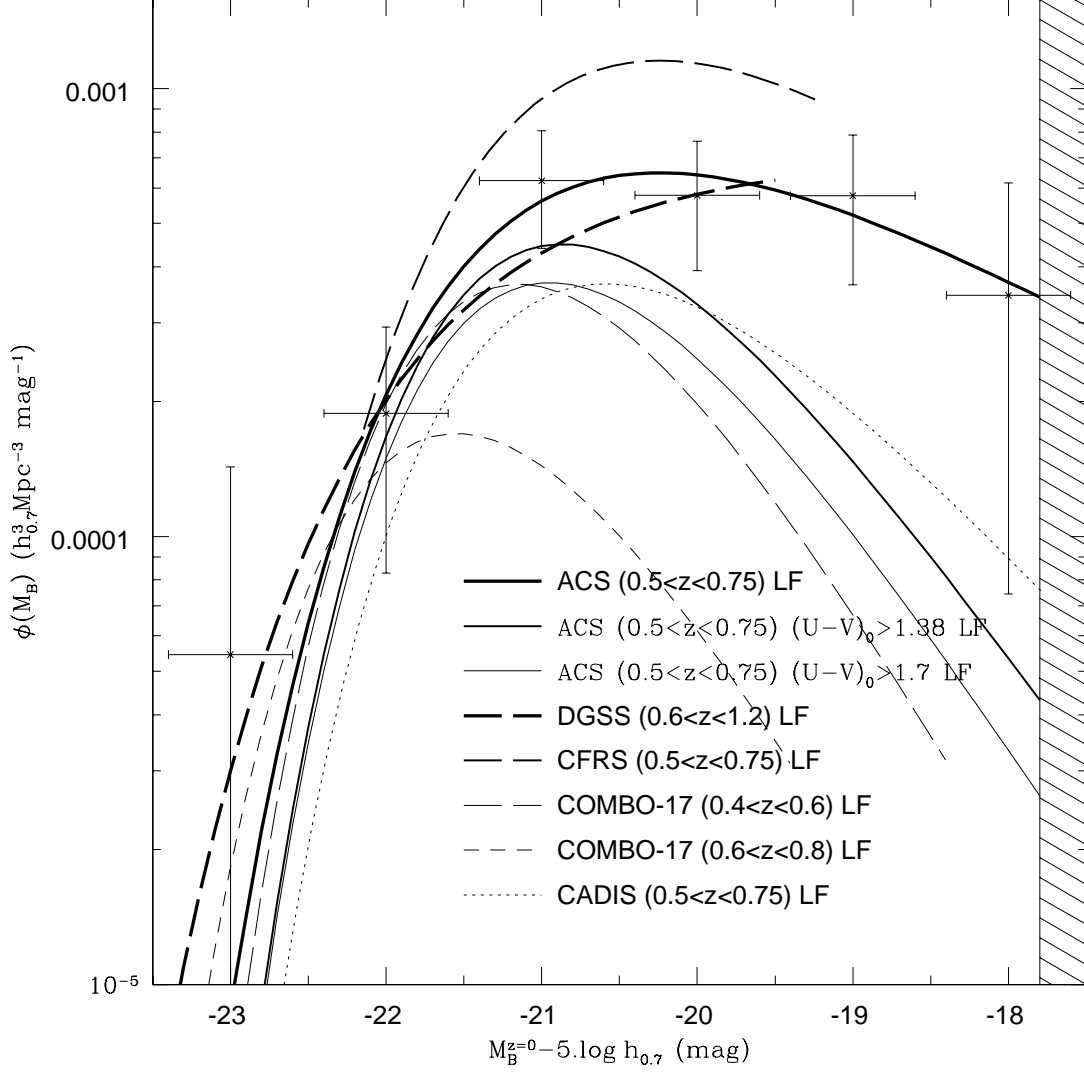


FIG. 17.— The luminosity functions of our  $0.5 < z < 0.75$  early-types compared to that from previous surveys. The ACS LFs are plotted with solid lines, with the thickest showing the morphologically selected LF, the medium thick showing the  $(U - V)_0 > 1.38$  LF and the thin line the  $(U - V)_0 > 1.7$  LF. The points and errorbars are for the morphologically selected sample. The thick dashed line shows the morphologically selected DGSS LF, the medium thick dashed line shows the  $(U - V)_0 > 1.38$  selected CFRS LF and the thin dotted or dashed lines show the SED selected COMBO-17 and CADIS LFs. All the luminosity functions have been converted to a  $\Lambda$ -CDM cosmology with  $H_0 = 70 \text{ km s}^{-1} \text{ Mpc}^{-1}$ .

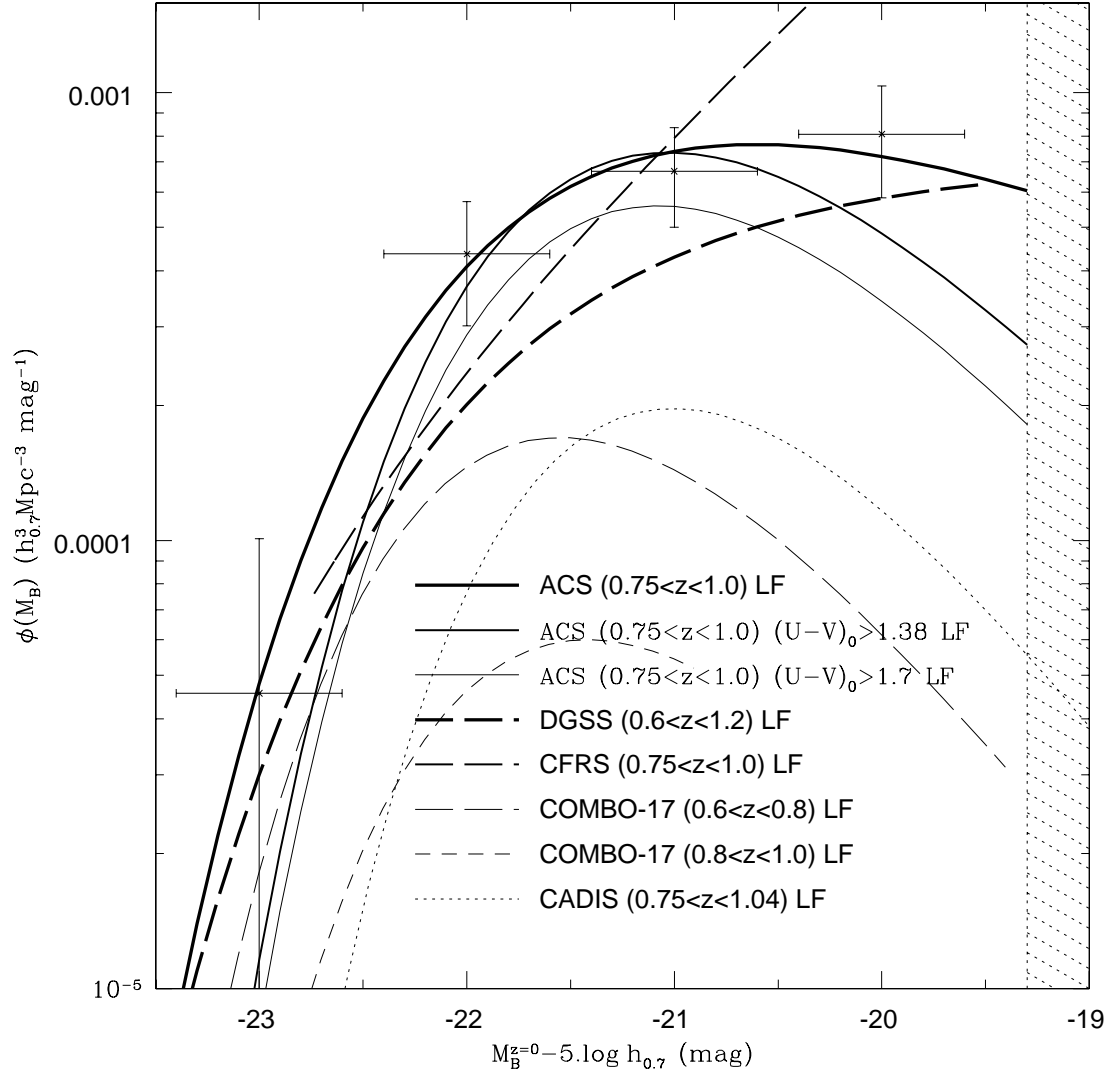


FIG. 18.— The luminosity functions of our  $0.75 < z < 1.0$  early-types compared to that from previous surveys. Otherwise, the same as Fig. 17.

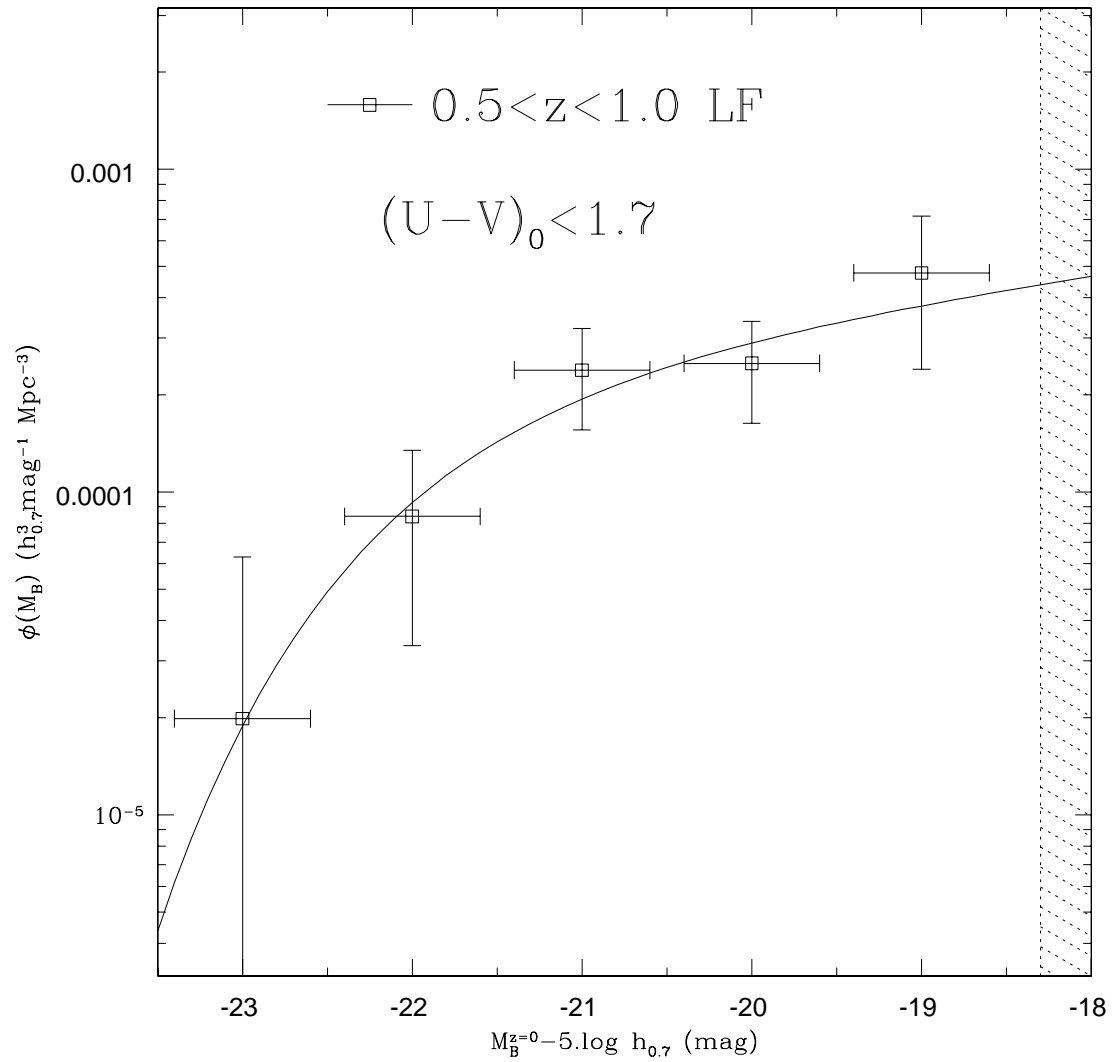


FIG. 19.— The luminosity functions of our  $(U - V)_0 < 1.7$  galaxies. The  $0.5 < z < 1.0$  LF is shown by square points with the solid line representing the best fit Schechter function, see Table 5.

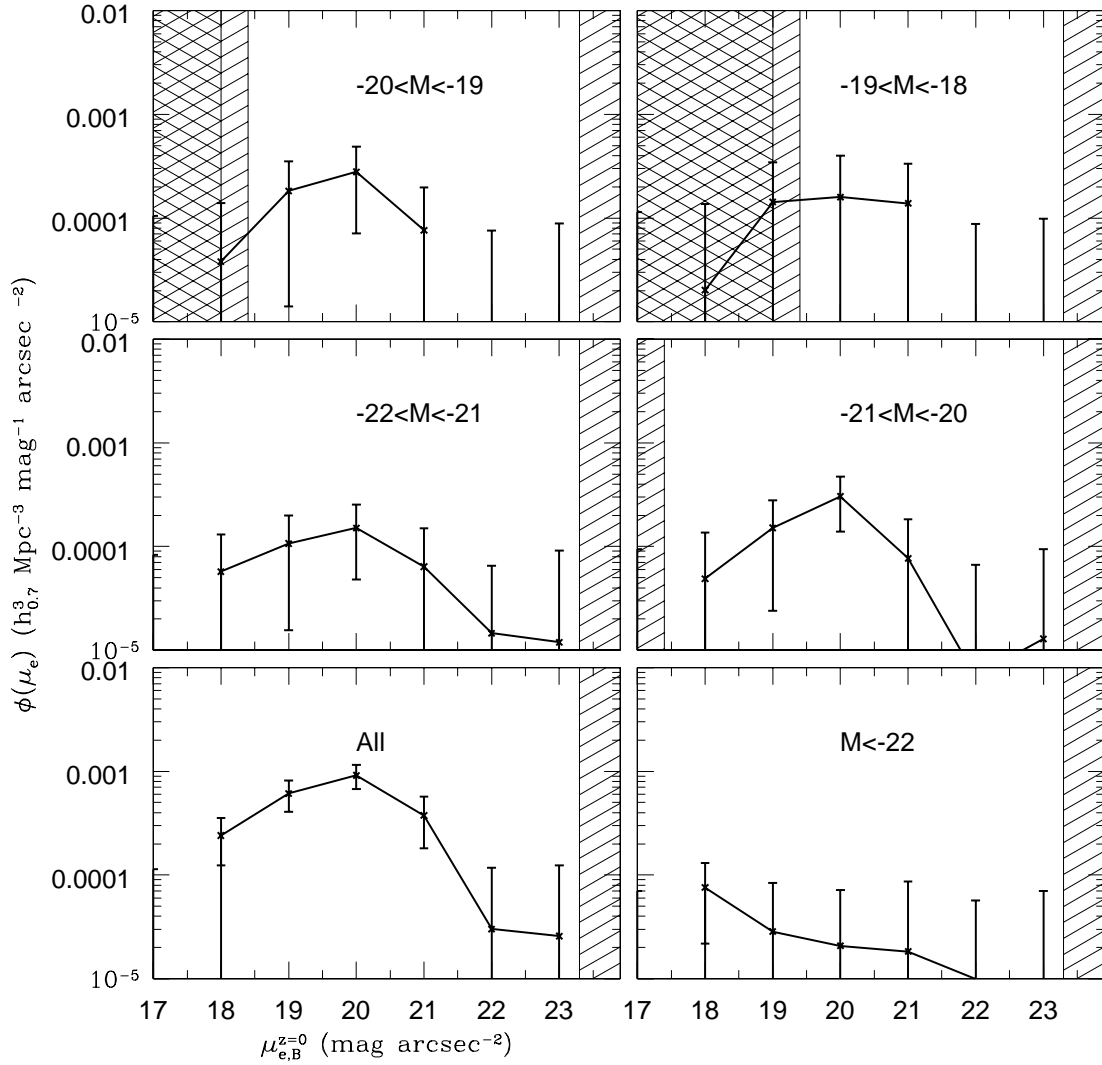


FIG. 20.— This plot shows the surface brightness distributions as a function of absolute magnitude for the  $0.5 < z < 0.75$  sample. The bottom left hand plot shows the surface brightness distribution summed to  $M_B = -18$ , close to the magnitude limit of the survey. The other 5 plots show the surface brightness distribution in small ranges of absolute magnitude. The shading represents the limits at the midpoint of all these magnitude ranges. The light shading is the region where the sample volume decreases from the maximum and the dark shading shows where there sample volume is zero.

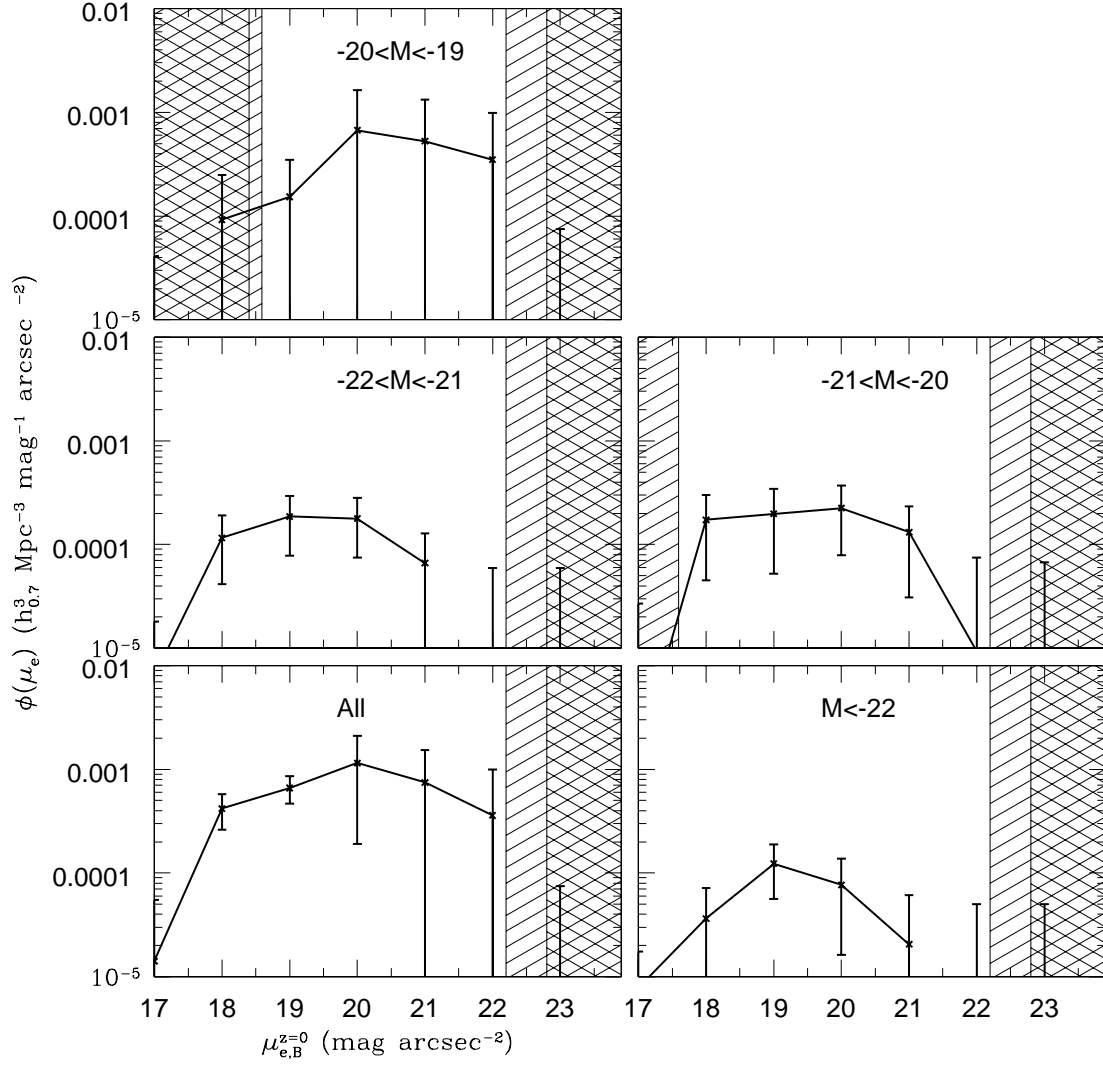


FIG. 21.— This plot shows the surface brightness distributions as a function of absolute magnitude for the  $0.75 < z < 1.0$  sample. The bottom left hand plot shows the surface brightness distribution summed to  $M_B = -19$ . Otherwise, the same as Fig. 20.